Dong Zhang · Jun-Duo Zhang · Wei-Xi Huang

Physical models and vortex dynamics of swimming and flying: a review

Abstract The swimming of aquatic animals and flying of insects and birds have fascinated physicists and biologists for more than a century. In this regard, great efforts have been made to develop new features and promote their applications in underwater and air propulsion. However, many challenges remain in understanding these forms of physical processes. Five key physical models are summarized to show how researchers use numerical and experimental methods to understand physiology, movement ecology and evolution from the viewpoint of fluid mechanics. They are morphological model, flexibility model, kinematics model, tethered/free model and force measurement model. Then, the latest progresses on the vortex dynamics of some simplified models and even high-fidelity models are presented, including the forming, growth, interaction, role and influence factors of the vortical structures. Some other aspects in swimming and flying, including stability, manoeuvrability and acoustics, are also briefly reviewed. Finally, the major challenges and several open issues in this field are highlighted.

1 Introduction

Studies of swimming hydrodynamics and flying aerodynamics have attracted considerable attention in recent years, as engineers and biologists have focused on the emerging field of biomimetics, in particular biorobotics of fish, insect and bird, with the aim of applying them in unmanned underwater vehicles (UUVs) [1] and micro-air vehicles (MAVs) [2] that can perform autonomous swim and flight in a natural environment. With over millions of years of evolution, natural swimmers and fliers are more efficient, manoeuvrable and quieter. Clearly, the performance of present man-made machines is far behind that of natural animals. In order to bridge this gap in performance, further advancement is required in our understanding of the hydrodynamics and aerodynamics of swimming and flying.

Many review papers and books have provided an overview of aquatic locomotion and airborne flight, from the classic works by Gray [3] and Videler [4], which provided a comprehensive portrait of fish swimming, to more recent overview volumes [5–10]. Also, works focusing on more specific topics can be found, such as the aspect-ratio studies on insect wings [11], flapping wing aerodynamics and aeroelasticity [12], undulatory and oscillatory swimming of aquatic animals [13], theories about swimming and flying [14], biomimetic survival hydrodynamics and flow sensing [15], flapping or bending of a flexible planar structure [16], passive and active

D. Zhang · J. Zhang · W. Huang (✉)
AML, Department of Engineering Mechanics, Tsinghua University, Beijing 100084, People's Republic of China
E-mail: hwx@tsinghua.edu.cn

D. Zhang
E-mail: dong_zhangyx@126.com

J. Zhang
E-mail: zhangjd18@mails.tsinghua.edu.cn

flow control by aquatic animals [17], drag reduction specific to dolphins [18] and hydrodynamics of jellyfish swimming [19].

The works above employed a large variety of models in theoretical, experimental and numerical studies; however, a systematic summary of these physical models is still lacking. The underlying physics of vortex helps us to understand how animals achieve high thrust and lift, such as the leading-edge vortex mechanism [20], but our knowledge is still limited, especially for the trailing-edge vortex and tip vortex mechanisms, which have attracted less attention. Our aim here is to supplement this body of works with a contemporary perspective on our understanding of the preferred models and fundamental fluid dynamics of swimming and flying.

2 Physical models of swimming and flying

Biology is evidently rich with complexity, encompassing a vast range of body morphologies and swimming/flying styles. Aquatic and flying animals propel themselves by fins, wings and bodies. Usually, the motion of the wings is used to produce enough lift for flight to support the flyer's weight, while the fins and bodies of underwater swimmers are used to produce thrust to overcome their drag. Generally, the morphology and kinematics vary with species; for example, the planform sizes of swimming and flight are different. An aerial flapping wing is usually too large underwater and an aquatic fin is too small for air [21]. As for kinematics, the locomotion of aquatic animals is divided into four main classifications, i.e. undulatory, oscillatory, pulsatile and drag-based [13]. Generally, undulatory swimmers pass more than one wave present on the fins at a time, whereas oscillatory swimmers display less than half a wave [22]. The body of the latter is held to be relatively stiff and is more similar to flying animals, which flap their wings to generate the needed lift. Pulsatile swimmers propel themselves by discharging water out of their body impulsively. Drag-based swimmers such as ducks and turtles propel a bluff body through water to generate thrust. Our principal consideration here will be the first two. Moreover, flexibility is one of the characteristics of animal fins/wings; fine musculature and compliant membranes allow both active and passive control of fin kinematics [23]. In order to understand the fluid mechanics of these animals, precise models need to be built to describe these complex motions. Here, we give a review of the physical models associated with these different propulsion patterns.

2.1 Morphological model

2.1.1 Simplified morphological model

The most widely used morphological model for swimmers and fliers is an airfoil [24–30], because the shapes of the propulsors of some swimming and flying animals closely resemble foils. As shown in Fig. 1, for undulatory swimmers, such as zebrafish [31] (Fig. 1a), the streamlined body shape seems like a symmetrical airfoil. Moreover, for some oscillatory swimmers (Fig. 1b, c) (such as sharks, whales, manta rays [32]) and birds (Fig. 1d) [33,34], the cross-sectional profile of their caudal fins and wings can be treated as a flapping foil. It is expected that most of the propulsion force generation is due to the fin/wing motion and the body is the main source of drag for those animals.

Most insects [35–37] and some fishes, such as bluegill sunfish [38] and tunas [39], have relatively thin fins and wings, which can be represented by a thin plate. Moreover, the plate model can be simplified into a two-dimensional (2D) filament [40–42], which is widely employed to investigate the motion of the fin/wing section or the body centreline. Other similar simplified morphological models contain rods and bars [43].

2.1.2 Morphological model of swimming

The simplified models have provided a good avenue for analysing simpler biological systems that contain the key mechanisms of real animals, such as leading-edge vortex (LEV) mechanism and trailing-edge vortex (TEV) mechanism, which will be introduced in Sect. 3. However, the effects of shape and three dimension influence the fluid and vortex dynamics significantly [44–46]. Real animals are complex in three dimensions, and the section shape varies along the body length. These features are not well represented by a simplified morphological model. With the development of scanner, imaging and surface construction technology [47], many high-fidelity morphological models were developed, which more closely approximate the real biological characteristics.
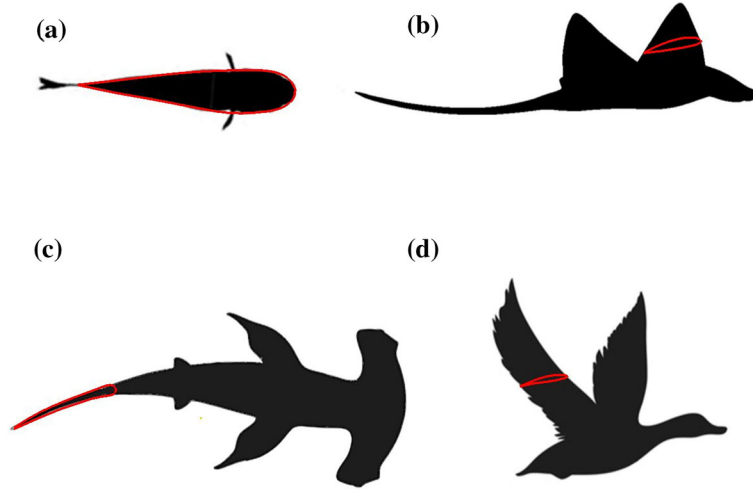
Fig. 1 Schematics of **a** zebrafish, **b** manta ray, **c** shark, and **d** goose, where the body of (**a**), the tail of (**c**) and the section profiles of (**b**) and (**d**) can be regarded as an airfoil

Kern and Koumoutsakos [48] gave an analytical description of a three-dimensional (3D) geometry of the eel, as follows:

$$
w(X) = \begin{cases} \sqrt{2w_h X - X^2} & 0 \le X \le s_b, \\ w_h - (w_h - w_t)(\frac{X-s_t}{s_t-s_b})^2 & s_b \le X \le s_t, \\ w_t \frac{L-s}{L-s_t} & s_t \le X \le L, \end{cases} \tag{1}
$$

$$
h(X) = b\sqrt{1 - \left(\frac{X-a}{a}\right)^2}, \tag{2}
$$

where the model has an ellipsoid cross section, and $w(X)$ and $h(X)$ are the two half axes; L is the body length; and s_b and s_t are the division points between head, body and tail. Here, $w_h = s_b = 0.04L$, $s_t = 0.95L$, $w_t = 0.01L$, $a = 0.51L$ and $b = 0.08L$; the geometry is plotted in Fig. 2a. Zhu et al. [49] described the shapes of a tuna model (Fig. 2b) and a giant danio model. The profile of the tuna body is given as

$$
w(X)/L = \begin{cases} \pm 0.152\text{tanh}(6X/L + 1.8) & -0.3 \le X/L \le 0.1, \\ \pm(0.075 - 0.076\text{tanh}(7x/L - 3.15)) & 0.1 < X/L \le 0.7, \end{cases} \tag{3}
$$

where the body section is also assumed to be elliptical with a major to minor axis ratio of 1.5 and a major axis length is equal to $w(X)$. The caudal fin was constructed by several chordwise sections of the NACA 0016 shape. The leading-edge and trailing-edge profiles are determined by

$$
w(Z)_{LE}/L = 39.543 \mid Z/L \mid^3 -3.685(Z/L)^2 + 0.636 \mid Z/L \mid +0.7, \tag{4}
$$
$$
w(Z)_{TE}/L = -40.74 \mid Z/L \mid^3 +9.666(Z/L)^2 + 0.77, \tag{5}
$$

where $-0.15 \le Z/L \le 0.15$. Similarly, the profile of the giant danio body is given as

$$
w(X)/L = \begin{cases} \pm 0.152\text{tanh}(6X/L + 1.8) + p(X) & -0.3 \le X/L \le 0.1, \\ \pm(0.075 - 0.076\text{tanh}(6.3X/L - 3.08)) + p(X) & 0.1 < X/L \le 0.7, \end{cases} \tag{6}
$$

where $p(X) = 0.0975\text{tanh}(-(0.3 + X/L)/1.5) + 0.0975$, and the body section is assumed to be an ellipse with a ratio of 2.2. Tanaka et al. [50] constructed a 3D symmetrical dolphin model based on the data measured by a portable non-contact scanner, as shown in Fig. 2c. The cross-sectional shapes of the flippers, dorsal fin and fluke were shown in their work. The model data (.STL format) were shared as supplementary material in their paper. Huang et al. [51] constructed a 3D cownose ray model based on the section profiles of the real cownose ray [22], as shown in Fig. 2d.
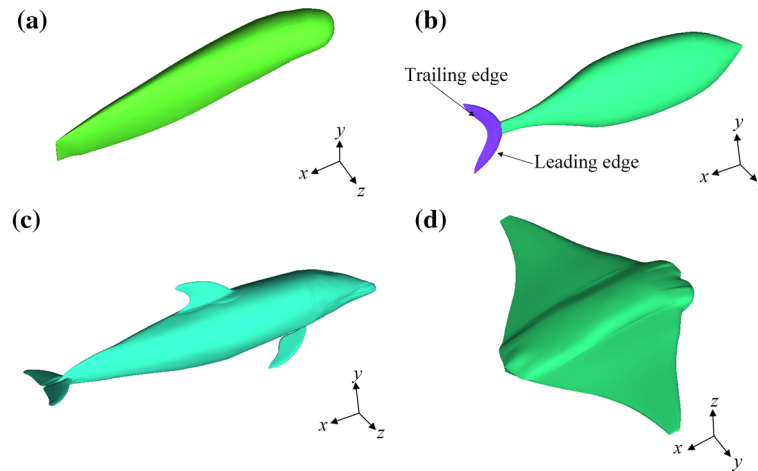
Fig. 2 The constructed morphological models of **a** eel, **b** tuna, **c** dolphin and **d** cownose ray. The morphological model description or STL format file is from Eqs. (1)–(2) [48], Eqs. (3)–(5) [49], Tanaka et al. [50] and Huang et al. [51]. Based on the above information, readers can easily construct their own morphological models

2.1.3 Morphological model of flying

For the fliers, the wing is usually assumed to have zero thickness. Thus, the morphological model can be easily obtained through the top view without the cross-sectional profile. Zou et al. [52] constructed the wing morphologies of a dragonfly and a damselfly. The top view of the two models is displayed in Figs. 3a, b, respectively, in which the head, thorax and abdomen are represented by an axisymmetric rotation. The fruit fly, bumblebee and hawkmoth [53–55] are also employed as the most common models for insect research, and the geometric outlines are shown in Figs. 3c–e. Liu et al. [56] constructed a mosquito wing model (Figs. 3f) extracted from microscopic images of recently excised wings and a body shape approximated from silhouettes of their own videos. Watts et al. [57] gave the plan view of the ventral surface of a bat wing, and the outline was used to build a 3D surface model (Fig. 3g) [58,59]. Using high-speed cameras, Maeda et al. [60] constructed a hummingbird wing model (Fig. 3h) which precisely captures the feathers and the cross-sectional bending.

The model data of the above swimming and flying animals were also included in their papers. We reconstructed these models as shown in Figs. 2 and 3. Most models from the above articles were given as mathematical descriptions, or the readers can easily construct theirs from the cross-sectional information.

2.2 Flexibility model

2.2.1 Active and passive flexibility model

The swimming and flying motions are fluid–structure interaction (FSI) processes. Swimmers and fliers flex their bodies, fins and wings to change their shapes either actively or passively. Generally, the body of aquatic animals is made of muscles, skeletons and cartilaginous tissues. Muscle actions are known to provide the actuation of body deformation. Thus, a high proportion of muscles makes some fishes, such as eels and batoid fish, use active rather than passive flexibility to precisely control the shapes of their fins and bodies to swim and manoeuvre. In the numerical studies of these animals, a flexible body shape is usually prescribed as an explicit deformation, which assumes that the passive deformation is much smaller than the active deformation. The prescribed deformation function will be introduced in Sect. 2.3.

There are many situations of passive flexibility, where investigations rely on a predetermined motion input (such as heave or pitch) and allow the flexibility of the model to determine its response. For example, the wings of insects are a membranous structure reinforced by the vein network [61]. The actuation acts at the wing root, and the wing deformation is a result of the inertial force, elastic force and aerodynamic force. The network of veins plays a supporting role and changes the stiffness distribution of the wing. Similarly, the wings of birds are bone–feather structures [62]. The bones are actuated by the smooth muscles to control the wing motion, whereas the feathers deform during flight due to their structural flexibility instead of active manipulation. The
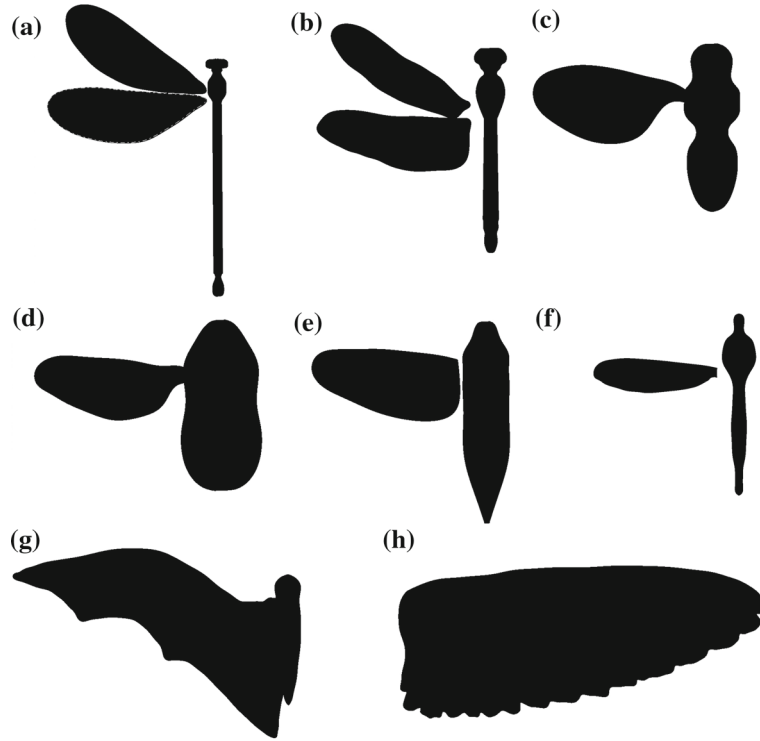
Fig. 3 Top view of the wing models of **a** dragonfly, **b** damselfly, **c** fruit fly, **d** bumblebee, **e** hawkmoth, **f** mosquito, **g** bat and **h** hummingbird. We constructed the models using the data obtained from [52–57,60]

finlets of tuna are attached to the body anteriorly with both muscular and skeletal supports but are separated from the body along their length [39]. So the anterior finlets can actively deform, whereas the rest part exhibits a level of passive flexibility. In these cases, the fluid–structure interaction accounts for the deformation response.

2.2.2 Simplified passive flexibility model

The most widely used passive flexibility model is a flexible plate or flag. To understand the fluid–flag interactions, Huang and Sung [63] examined the flag motion undergoing passive flapping in a uniform flow. The flag motion is solved using the structure motion equation, as follows:

$$\rho \frac{\partial^2 X}{\partial t^2} = F_e + \rho g - F, \tag{7}$$

where X is the displacement, ρ denotes the extra flag area density, g denotes the gravity, F denotes the Lagrangian forcing exerted on the flag by the surrounding fluid and F_e denotes the elastic force obtained by using the energy method. The elastic energy can be expressed as follows:

$$E(X) = \int_s \sum \left[c_{ij}^T (T_{ij} - T_{ij}^0)^2 + c_{ij}^B (B_{ij} - B_{ij}^0)^2 \right] ds_1 ds_2, \tag{8}$$

where (s_1, s_2) is the curvilinear coordinate system, T_{ij} denotes the stretching and shearing effects, B_{ij} denotes the bending and twisting effects, c_{ij}^T and c_{ij}^B are the corresponding coefficients and the superscript '0' denotes the initial state. Then, the elastic force is obtained by the derivative of the energy, as follows:

$$F_e = \sum \left[\frac{\partial}{\partial s_i} \left(\sigma_{ij} \frac{\partial X}{\partial s_j} \right) - \frac{\partial^2}{\partial s_i \partial s_j} \left(\gamma_{ij} \frac{\partial^2 X}{\partial s_i \partial s_j} \right) \right], \tag{9}$$

where $\sigma_{ij} = 4c_{ij}^T (T_{ij} - T_{ij}^0)$ and $\gamma_{ij} = 2c_{ij}^B$. The fluid motion is determined by solving the Navier–Stokes equations, and the immersed boundary method [64,65] is adopted to deal with the fluid–structure interaction. Similar models can be also found in [66–68].
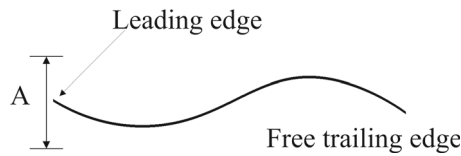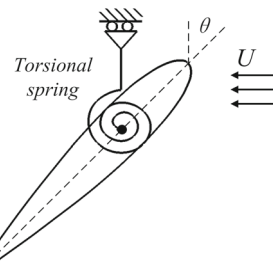
Fig. 4 Schematic of the flexible flag model

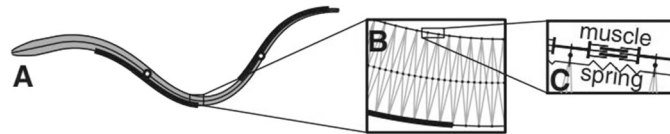**Fig. 5** Schematic of a reduced flexibility model: torsional spring model

Fig. 6 Schematic of the flexibility model of a lamprey. Adapted with permission from [79]

The flag has a fixed leading edge and a free trailing edge, i.e. the model undergoes entire passive deformation without any active input. Similar models are used with different boundary conditions to check the propulsion mechanism of flexible bodies. As shown in Fig. 4, the leading edge of the flag is forced to heave vertically and sinusoidally, which is used to mimic the motions of insect/bird wings and fish fins for locomotion through fluids. Using the above passive flexibility model, a variety of numerical studies [41,42,69,70] have been conducted. Moreover, the 3D plate can also be simplified into a 2D case [71].

Another widely used simplified model is the torsional spring model. It produces the effect of torsional flexibility assumed to be lumped into a spring, and the torsional stiffness is characterized by the spring constant. The schematic of the torsional spring model is shown in Fig. 5, and it is usually associated with a rigid foil or wing [72–78].

2.2.3 Passive flexibility model of swimming

To examine the roles of body stiffness, muscle activation and fluid dynamics in swimming animals, Tytell et al. [79] constructed a lamprey model built with three segmented filaments, i.e. a stiff centreline and two lateral sides, as shown in Fig. 6. The lines are connected with several links to mimic the muscular forces delivery. The links along the centre filament and the cross links which connect the centreline to the lateral sides are modelled as passive Hookean springs. The links along the lateral sides do not resist compression. There are some active flexible regions (thick lines) that mimic the activated muscle. The activation pattern is prescribed based on the lamprey kinetic model. The active flexible region travels down along the body like an activation wave. Only 30% of the body is active at any given time.

2.2.4 Passive flexibility model of flying

The above model employs uniform flexibility. By measuring the flexural stiffness in the forewings of 16 insect species, Combes and Daniel [80] found that the wing is stiffer in the spanwise direction than in the chordwise direction. Shahzad et al. [81] built a finite element model of hawkmoth wing and conducted fluid–structure interaction simulations to check the effect of flexibility on the aerodynamic hovering performance. As shown in Fig. 7, the veins and membrane are discretized by triangular elements. The material stiffness of the vein elements is increased beyond that of the surrounding membrane to produce spanwise–chordwise anisotropy
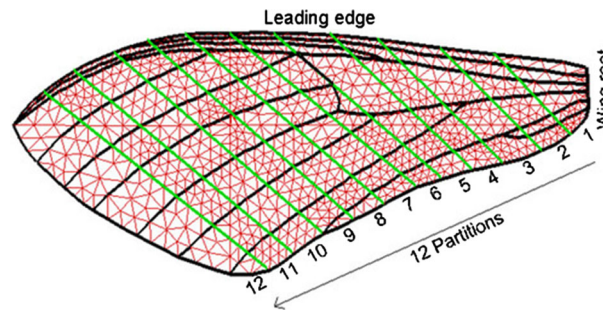
Fig. 7 Schematic of the flexibility model of a hawkmoth's forewing, showing the distribution of veins and partitions. Adapted with permission from [81]

Table 1 The parameters of various BCF kinematics

Species	$A(x)$	λ	Ref
Anguilliform	$0.0367 + 0.0323x + 0.0310x^2$	0.5–1	Khalid et al. [83]
Anguilliform	$0.125(x + 0.03125)/1.03125$	1	Kern et al. [48]
American eel	$0.0699e^{2.76(x-1)}$	0.6	Tytell [84]
American eel	$0.1e^{x-1}$	0.642	Borazjani et al. [85]
Carangiform	$0.00236x - 0.63x^2$	0.89–1.1	Borazjani et al. [86]
Tuna	$0.02 - 0.08x + 0.16x^2$	1.38	Zhu et al. [49]
Tuna	$0.01617 - 0.06311x + 0.1369x^2$	1.25	Zhang et al. [87]

in flexural stiffness. Moreover, the insect wings are more flexible towards the tip. This effect is incorporated by employing a declining value of Young's modulus in the partitions (from 1 to 12) from the wing root to the tip. The material properties in the partitions are addressed in [81].

2.3 The kinematic description

For the active flexibility models, the deformations are usually prescribed as kinematic descriptions. This kind of model provides an approach to investigate the direct effect of kinematics of animals on the fluid mechanics without considering the body mechanics because the prescribed function can be controlled precisely by adjusting the function parameters. Generally, the kinematics are collected from experimental work of real fliers and swimmers. By simplification and assumptions, we can obtain some mathematical functions to describe the kinematics model.

2.3.1 Swimming animal

Fish locomotion can be classified into the body/caudal fin (BCF) mode and the median/paired fin (MPF) mode [32,82], according to the propulsion part. For the BCF swimmers, the lateral position of the centreline could be described as, after normalization by using the body length, as follows:

$$Z(X) = A(X)\sin\left(\frac{2\pi}{\lambda}X - 2\pi ft\right), \tag{10}$$

where X denotes the streamwise coordinate of the fish centreline, f is the oscillation frequency, t is the time, λ is the wavelength and $A(x)$ is the oscillation amplitude in the lateral direction. The kinematics model assumes that a travelling wave travels along the fish body. The value of λ and the expression of $A(x)$ have been observed to change among different swimming modes. Note that the wavelength, λ, is a criterion to distinguish the swimming styles of undulatory and oscillatory swimmers. Undulatory swimmers have a wavelength equal to or shorter than their body length ($\lambda \leqslant 1$), whereas the wavelength of oscillatory swimmers are longer than their body length ($\lambda > 1$). The amplitude envelop, $A(x)$, is depicted by a polynomial or exponential function. A summary of $A(x)$ and λ for different swimmers is listed in Table 1.
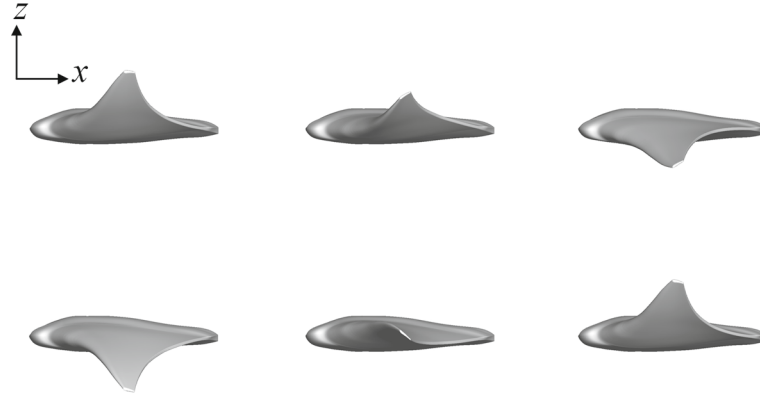
Fig. 8 Motion of a cownose ray pectoral fins at six time instants

For the BCF oscillatory swimmers, the thrust generation is primarily due to the prominent caudal fin. Due to the longer wavelength compared with the body length, the caudal fin describes a combination of heaving and pitching motions. The pectoral fin movement of some MPF swimmers, such as manta ray, can also be regarded as an assembly of several similar motions. The heaving and pitching functions can be described by sinusoidal motions with a common frequency, as follows:

$$h = h_0 \sin(2\pi f t), \tag{11}$$

$$\theta = \theta_0 \sin(2\pi f t + \phi), \tag{12}$$

where h_0 is the heave amplitude, θ_0 is the pitch amplitude and ϕ is the phase difference between pitch and heave. The investigation of the movements of pure pitching, pure heaving and a combination of heaving and pitching can be found in [88–93].

Actually among the MPF swimmers, the deformations of batoid fishes, with dorsoventrally flattened bodies and expanded pectoral fins are more complex. Batoids propel themselves by moving their enlarged pectoral fins in a flapping motion (spanwise flexing), combined with a travelling wave motion (chordwise flexing). Zhang et al. [94] described the flapping motion of a cownose ray, taking both the spanwise and chordwise deformations into consideration, as follows:

$$
\begin{aligned}
X(X_f, X_f, t) &= X_f, \\
Y(X_f, Y_f, t) &= Y_f(1 - (1 - k)|f(X_f, t)|Y_f/SL)\cos[\theta_{\max}Y_f/SL \cdot f(X_f, t)], \\
Z(X_f, Y_f, t) &= Z_f + Y_f(1 - (1 - k)|f(X_f, t)|Y_f/SL)\sin[\theta_{\max}Y_f/SL \cdot f(X_f, t)], \\
f(X_f, t) &= \sin(\omega t - 2\pi \frac{BL}{\lambda} X_f/BL),
\end{aligned}
\tag{13}
$$

where (X_f, Y_f) defines the neutral plane of the pectoral fins in a flat position without deformation, as shown in Fig. 2d; (X, Y, Z) represents deformed coordinates at time t; and the body length and span length are represented by BL and SL, respectively. A travelling wave with a wavelength of λ is used to present the chordwise deformation; ω is the angular frequency, while k and $\theta_{\max}$ are parameters making the deformation to fit the biological measurements along the entire span. Taking a tip-to-tip amplitude of $0.7BL$ as an example, it can be determined that $\theta_{\max} = 0.488169$ and $k = 0.960779$. The flapping motion is displayed in Fig. 8.

Thekkethil et al. [95] presented the kinematics model for the various types of batoid fish-like body by varying the wavelength of chordwise undulation, as follows:

$$Z = \frac{A_{\max}X|Y|}{0.5A_R}\sin[2\pi(X/\lambda^* - St\tau/2A_{\max})], \tag{14}$$

where Z is the vertical displacement, X and Y are the streamwise and spanwise coordinates, respectively, τ is the non-dimensional time, A_R is the aspect ratio of the body, $St = f a_{\max}/u$ is the Strouhal number with $a_{\max}$ the maximum amplitude and $A_{\max}$ its non-dimensional value and λ^* is the non-dimensional wavelength. The parameters of $A_{\max} = 0.15$, $\lambda^* = 4, 1.2, 0.8$ were employed to mimic the motion of Dasyatis, Gymnura micrura and Rhinoptera bonasus, respectively.

Bottom II et al. [96] described the kinematics of a swimming stingray (MPF undulatory swimmer), as follows:

$$
\begin{aligned}
Y(t) &= A_Y(X, Y)\cos(2\pi/\lambda X - 4\pi f t), \\
Z(t) &= A_Z(X, Y)\cos(2\pi/\lambda X - 2\pi f t),
\end{aligned}
\tag{15}
$$

where A_Y and A_Z are the amplitudes in the lateral and vertical directions, respectively. Body and pectoral undulations are measured for 31 points on the stingray [97], and then, the amplitudes were obtained based on a least-squares approximation. The computation of these parameters can also be found in [98].

For some more complex kinematics, the points on the wing/fin surface are tracked, and the time histories of these points can be used directly as the input of computational work without an analytical description. The bluegill sunfish's pectoral fin kinematics during steady forward motion was constructed using the direct linear transform (DLT) algorithm [99,100]. About 20 time frames and 280 total points per frame were digitized for the fish. Then, a cubic spline interpolation was employed to obtain finer surface mesh points and that at a much higher frame rate required for CFD.

2.3.2 Flying animal

For the flying animals, their kinematics are always regarded as the combination of translation and rotation of plates; thus, the active deformation of their motions can be prescribed as the time histories of the three Euler angles, i.e. the orientation of the wing in the stroke plane, which is defined as follows: By projecting the wing-tip points of both the left and right wings to the body symmetry plane, a linear regression line of the projection can be determined. The plane passing through the wing root and parallel to this line is defined as the stroke plane. As shown in Fig. 9, the stroke angle, ϕ, denotes the angular displacement of the wing in the stroke plane; the deviation angle, θ, is defined as the angle between the root-to-tip line of the wing and the stroke plane. It represents the rotations with respect to the stroke plane; the wing pitch angle, α, is the angle between the wing chord and the tangent of the wing trajectory.

The time histories of the Euler angles of hovering mosquito [56], hummingbird [101], dragonfly [102] and cicada [103] are shown in Fig. 10. For most birds, the stroke plane angle is close to 90°, whereas the stroke plane angle of insects is close to 0° [104]. Thus, the wing-tip trajectory of birds in the global coordinate system is more like an up–down motion, whereas that of insects is like a front–back motion. From the Euler angles evolutions, the motion of fliers is asymmetrical, compared with that of the swimmers. Note that mosquitoes are special in that they have a very small stroke amplitude. Besides, they generate a fast-pitching-up rotation [56]. The pitching angle increases rapidly, pitching up from about 16° to 46° ($t/T = 0.12 - 0.34$), whereas for other insects with a large stroke amplitude, the pitching angle changes only slightly. Because the wing of mosquito has spanwise variation in pitch angle (wing twist) during the flapping motion, the authors introduced the attack angle difference at the wing root and at the wing tip($\triangle\alpha$) to represent the spanwise change in pitch angle. The kinematics of some special behaviours of fliers have also been studied, such as a dragonfly in takeoff flight [37], turning flight [105], backward free flight [106] and the reverse flight of a butterfly [107].

2.4 Tethered and free swimming/flying model

In terms of the degrees of freedom, researchers have used two kinds of models, i.e. tethered and free models. The tethered model enables the free movement of the fin or wings at a fixed position and attitude. One benefit of this model is that it is easy to measure the forces produced by the model and to visualize the flow field. Some
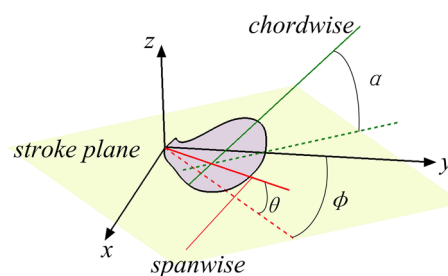

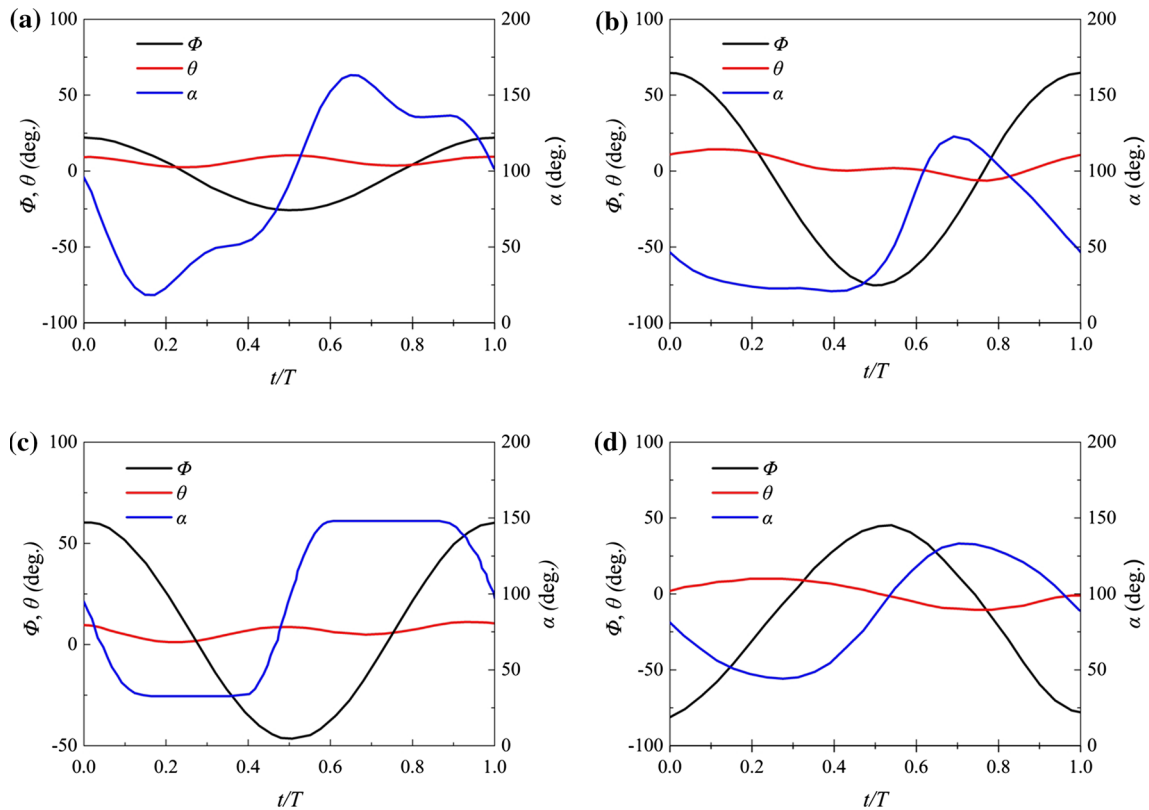**Fig. 9** Definition of the Euler angles for flying animals

Fig. 10 Time histories of Euler angles of **a** mosquito , **b** hummingbird, **c** dragonfly and **d** cicada. The data are obtained from [56,101–103]

experimental works [108–110] using tethered models are available. Tethering allows for higher-quality flow visualization results, as the relative position and orientation of the animal and the measurement region can be precisely adjusted, and it is sufficient to identify critical points in the flow [111]. However, tethering can also lead to unnatural wing motions and, thus, may not be representative of the real flying and swimming state. Thomas et al. [111] performed the first extensive flow visualizations of free-flying dragonflies. Afterwards, free-flight measurements were conducted with bumblebees [112], bats [113], hummingbirds [114], etc. The flow fields of free swimming have also been widely investigated [115–117].

In numerical studies, the weaknesses of the tethered model have been eliminated because the kinematics in simulations are not disturbed by outside environment. We should point out some differences between the two models here. Note that we only discuss the condition when a steady free swimming or flying speed reaches. Firstly, in the free swimming/flying model simulation, the information of the model speed and the flow field can easily be obtained. However, it is hard to obtain the thrust or lift force of the propulsors because the thrust is balanced with the drag force. The thrust characteristics can be easily obtained through the tethered model by adjusting the inflow condition and kinematics, just like a propeller open water experiment. Secondly, the tethered model is used in a free-stream inflow. By adjusting the inflow, if the net mean force becomes zero, making constant-speed self-propulsion possible, the tethered model is regarded to be representative of the free model at such condition [86]. In fact, the speed of the free model is produced as a result of the thrust and drag, but it is not fixed. The speed usually has an oscillation around its mean value [45,96]. For this reason, the inflow at the tethered condition cannot reflect the real speed at the free condition. Van Buren et al. [118] demonstrated that velocity oscillation and variation have little influence on the thrust performance of oscillating foils, which indicates that the performance characteristics of the tethered model can be representative of that of the free model. Note that their experiment employed an isolated propulsor. For a body-fin/wing system, the body is the main source of drag. The drag characteristics of the body vary with the speed; thus, the total force characteristics of the two models are different. Smits [13] pointed out the importance of lateral velocity over swimming speed as the correct velocity scale; it can largely erase the difference between the results obtained in the tethered and free-swimming models.

2.5 Measures of swimming/flying performance

2.5.1 Force coefficients

We are particularly interested in the thrust and lift coefficients of swimming and flying animals. The results of propulsive performance are usually presented in non-dimensional form, as follows:

$$C_{T,L} = \frac{F_{T,L}}{0.5\rho U^2 L^2},$$

(16)

where F_T and F_L represent the net thrust and lift force, respectively, ρ is the fluid density and U and L are the speed and length of the animal, respectively. Note that the net thrust, F_T, is often given as the thrust F_x (the streamwise component of the force developed by the motion) minus the drag force, D_p, i.e.

$$F_T = F_x - D_p.$$

(17)

This definition is more suitable for isolated propulsors, such as oscillating foils or plates. Just like the relationship between a propeller and a ship, animals can be treated as a body + propeller system. So for such a whole system, the net thrust includes the drag of the body, i.e.

$$F_T = F_x - D_p - D_B.$$

(18)

2.5.2 Net efficiency (η_n)

Efficiency in its strict definition is the output power divided by the input power, i.e.

$$\eta = \frac{\overline{P_{\text{out}}}}{\overline{P_{\text{in}}}}.$$

(19)

Here, we need to give an introduction and discussion of various definitions of powers and efficiency. The first definition is the net propulsive efficiency η_n, where the output and input powers are computed, respectively, as follows:

$$\overline{P_{\text{out}}} = \overline{F_T} U,$$

(20)

$$P_{\text{in}} = P_{\text{musc}} = \int_{\Omega} \boldsymbol{F} \cdot \boldsymbol{U}_{\text{body}} ds,$$

(21)

where P_{musc} represents the power actuating the movement of the swimmer's body surface, which is the vector product of the force to actuate the fins, $\boldsymbol{F}$, and the deformation velocity, $\boldsymbol{U}_{\text{body}}$, at each boundary element, ds.

This definition is traditionally used to measure the performance of an isolated propeller, i.e. the use of Eqs. (17) and (20) to compute the output power. The definition represents the propulsor efficiency, whereas it represents the swimming efficiency using Eq. (18). The swimming efficiency here means the whole hydrodynamic efficiency of the body + propeller system. It is important to distinguish between the two definitions. The above definition of P_{out} is a meaningful measure of useful power output for an isolated propulsor. For an accelerating body + propeller system, e.g. a fish performing an escape manoeuvre, the definition is still a reasonable measure. However, for a body + propeller system, once the cruising speed is reached and the body moves at a steady speed, the thrust force is exactly equal to the drag force, resulting in zero efficiency. Moreover, when we use the tethered model at a low-Reynolds number or low-frequency/amplitude condition, it may be hard for the thrust to overcome the drag, which makes a negative efficiency. As shown in Table 2, the net efficiency of cownose ray at $St = 0.62$, $Re = 2200$ is -0.085. This negative efficiency means that a cownose ray would perform better without the undulatory motion of the pectoral fin. Obviously, this is a bad definition in such circumstance.
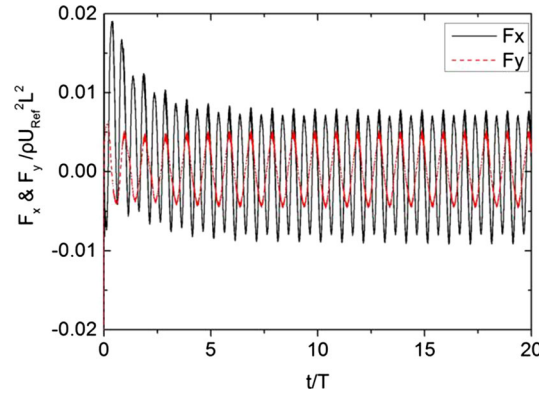
Fig. 11 Temporal evolution of the streamwise and lateral forces of a steady swimming eel. Adapted with permission from [45]

2.5.3 Froude efficiency (η_f)

For a steady swimming system, the Froude efficiency [119] is commonly used, where P_{out} is computed as

$$\overline{P_{\text{out}}} = \overline{D}U \tag{22}$$

and P_{in} is computed as

$$P_{\text{in}} = \overline{T}U + \overline{P}_{\text{musc}}, \tag{23}$$

where $\overline{D}$ and $\overline{T}$ are the mean drag and thrust forces of the swimmer, respectively, and $\overline{P}_{\text{musc}}$ has the same meaning with that in Eq. (21). Here, the output power is used to balance the drag power on a 'ship', and the input power is the total power gained by a swimmer from fluid, including $\overline{T}U$. Since drag is always equal to thrust during steady swimming, the efficiency is always less than one.

However, there exists a disadvantage for this definition. For some animals, we can identify a local part of the body, such as the caudal fin, as the main propeller, and the rest part as the main source of drag. For instance, at a Reynolds number of 2100, the caudal fin of an undulatory crevalle jack fish provides a thrust coefficient of 0.593, whereas the fish's trunk, dorsal fin and anal fin generate a drag coefficient of 0.6879 [120]. The total force generated by the dorsal and anal fins of a bluegill sunfish at a Reynolds number of 3000 is only 5% of the caudal fin force [121]. It is easy to obtain $\overline{D}$ and $\overline{T}$. In the cases of undulatory swimmers and batoid fishes, the drag and thrust producing regions are not distinct; thus, we need to separate the sources of body drag from the sources of thrust.

Subsequently, some approaches to separate the drag and thrust will be introduced. In the first approach, we estimate the drag and thrust by the direction of streamwise force. The streamwise force on an eel during steady swimming is shown in Fig. 11. The force oscillates about a zero mean value. Positive values may be interpreted as thrust and negative values as drag.

Borazjani and Sotiropoulos [122] used arbitrary decomposition to separate the thrust and drag forces:

$$T(t) = \frac{1}{2}\left(\int_A -pn_3 \mathrm{d}A + \left|\int_A pn_3 \mathrm{d}A\right|\right)$$
$$+ \frac{1}{2}\left(\int_A \tau_{3j}n_{j3}\mathrm{d}A + \left|\int_A \tau_{3j}n_j\mathrm{d}A\right|\right), \tag{24}$$

$$-D(t) = \frac{1}{2}\left(\int_A -pn_3 \mathrm{d}A - \left|\int_A pn_3 \mathrm{d}A\right|\right)$$
$$+ \frac{1}{2}\left(\int_A \tau_{3j}n_{j3}\mathrm{d}A - \left|\int_A \tau_{3j}n_j\mathrm{d}A\right|\right), \tag{25}$$

where $T(t)$ and $D(t)$ are the instantaneous thrust and drag forces, respectively, n_i is the ith component of the unit normal vector on $\mathrm{d}A$, the model swims along n_3, τ_{ij} is the viscous stress tensor and p is the pressure force. In some other studies, the pressure force may be regarded as the thrust sources [123,124]. The various approaches provide different ideas to separate drag and thrust; however, they also cause the problem of not

having a unified standard to measure the efficiency, because different approaches result in different efficiency values [125]. As shown in Table 3, for the free-swimming sting ray, manta ray and tuna, we calculated different Froude efficiencies for the different definitions of the thrust force.

2.5.4 EBT-based Froude efficiency (η_{EBT})

The third approach is Froude efficiency based on Lighthill's elongated body theory (EBT) [126]:

$$\eta_{EBT} = \frac{1}{2}(1 + U/V), \tag{26}$$

where U is the swimming speed and V is the wave speed of the undulatory body. Cheng and Blickhan [127] indicated that EBT overestimates the efficiency. As also shown in Table 3, the EBT efficiencies are higher than other definitions. However, the theory provides a simple way to evaluate the efficiency roughly [84,86].

2.5.5 Work-based efficiency (η_W)

By integrating the power over the undulation cycle in order to obtain the amount of work, W, done by the swimmer and using the kinetic energy, E, of the forward motion of the body to represent the output work, we can characterize the swimming efficiency, as follows [45,48]:

$$\eta_W = \frac{E}{W}, \tag{27}$$

$$E = \frac{1}{2}mU^2, \tag{28}$$

$$W = \int_t^{t+T} P_{\text{in}}\mathrm{d}t. \tag{29}$$

This definition replaces the definition of work based on the thrust and the swimming kinetic energy, and it avoids the computation of thrust force. A disadvantage of this definition is that efficiency is not necessarily less than one [45]. For instance, η_W of a sting ray is 276, which is significantly higher than other efficiencies, as shown in Table 3.

2.5.6 Quasi-propulsive efficiency (η_{QP})

Another approach uses the concept of quasi-propulsive efficiency [128], i.e.

$$\eta_{QP} = \frac{(\overline{F_T} + R)U}{\overline{P}_{\text{musc}}}, \tag{30}$$

where F_T is the net thrust as Eq. (17) or Eq. (18), and R is the towed resistance at speed U. The towed resistance must be measured or estimated in a straight configuration, without bending of the body. $\overline{P}_{\text{musc}}$ is the power required by the propulsor to drive the system at speed U. This definition can also be used in the swimming acceleration process. For the case of a self-propelled swimmer at a steady speed, $\overline{F_T} = 0$. Therefore, the efficiency can be written as follows:

$$\eta = \frac{RU}{\overline{P}_{\text{musc}}} = \frac{\overline{T}_p U}{\overline{P}_{\text{musc}}} \frac{R}{\overline{T}_p} = \eta_p \frac{R}{\overline{T}_p}, \tag{31}$$

where η_p is the propulsor efficiency. This definition is similar to that used in naval architecture [128], $\eta = \eta_p \eta_H$, where η_H is the hull efficiency which accounts for the hydrodynamic interference between the hull and the propeller. The quasi-propulsive efficiency is based on two separate experiments, one for a towed body to compute the useful power and the other for the self-propelled experiment to compute the input power. The advantage of this definition is the universality of efficiency, without worrying about drag and thrust separation in the free-swimming model. It can also give a reasonable estimation of the efficiency for the low-Re swimming, at which the model may swim at a negative efficiency, as shown in Table 2. On the other hand, the disadvantage is that with this kind of definition, the efficiency is not strictly less than one, e.g. that of tuna in Table 3, in the circumstance that the propulsor causes the body drag to drop substantially compared with that of the towed drag.

Table 2 Efficiency for various species using the tethered model

Species	St	Re	η_n	η_{QP}
Cownose ray [94]	1.3	2200	0.13	0.17
Cownose ray [94]	0.65	2200	−0.085	0.27
Tuna [87]	0.45	2000	−0.78	0.10

Table 3 Efficiency for various species using the free-swimming model. Here, η_{f1}, η_{f2} and η_{f3} are computed by the arbitrary decomposition from Eq. (24), streamwise force and pressure force, respectively

Species	St	Re	η_{f1}	η_{f2}	η_{f3}	η_W	η_{EBT}	η_{QP}
Sting ray [96]	0.34	13,500	0.23	0.15		276	0.88	
Manta ray [123]	0.39	Inviscid			0.48		0.99	
Tuna [86]	0.6	4000	0.23	0.97			0.67	73

2.5.7 Cost of transport

In life sciences, the fitness of a self-propelled system is traditionally measured by the cost of transport (COT) [129], defined as the energy spent per unit distance travelled:

$$COT = \frac{P}{mgU}, \tag{32}$$

where P is the metabolic rate and m is the mass of the animals. This concept is a more direct estimate of fitness than hydrodynamic performance. Moreover, some use the energy required to move a unit distance to measure the efficiency. The measurement of fish swimming energetics was reviewed by Lauder [5]. Bale et al. [130] indicated that when comparing the efficiencies of a whale and a tuna, the whale wins using the former, whereas the tuna wins using the latter. Therefore, a new efficiency called the energy consumption coefficient is introduced [130]:

$$C_E = COT \frac{\rho_b^{2/9}}{k_m^{2/3} \rho^{1/3} M^{2/3}}, \tag{33}$$

where ρ_b is the mean body density, k_m is a constant in the metabolic rate equation [130], ρ is the fluid density and M is the animal's mass.

Given a scaling of energy cost per unit distance travelled, this definition is applicable to swimming and flying animals and also to the terrestrial locomotion, automotive vehicles and self-propelled vehicles in general.

3 Vortex dynamics of flying/swimming

3.1 Leading-edge vortex (LEV)

3.1.1 Role of LEV in flying and swimming

To reveal the mechanisms of natural flapping flight, studies have been conducted through various approaches. A mechanism undiscovered in the steady flow has been identified by Ellington et al. [108]. Specifically, as the wing translates at a high angle of attack (AoA), the flow separates at the leading edge of the wing and forms the leading-edge vortex (LEV), which induces low pressure on the suction side of the wing and significantly contributes to the lift during the translation stage [10,131]. The LEV stably attaches to the wing during translation of multiple chords instead of stalling and developing into the von Kármán street in steady flow and 2D models [20]. Thus, this mechanism is also known as the delayed stall, or absence of stall [7]. The LEV is perceived as the most robust force enhancing mechanism that has been convergently employed by a wide range of creatures in nature. Although the LEV was first disclosed in insect flight, it has also been discovered in various forms of biological propulsion, including flapping flight with morphing wings of birds [33,132] and bats [133–135], revolving rigid plant seeds [136] and oscillating propulsor in fish [120] and bird [137]. Due to

its critical role in bionic flows, the LEV has been extensively reviewed in insect flight [10,131,138], extended to vertebrate flight [7] and summarized through the mechanism perspective [20].

In order to achieve a quantitative investigation of the role of the LEV on force production, the derivative-moment transformations (DMT)-based force expression is introduced here. In numerical work, the traditional method of computing the force exerted on a body is the integration of the pressure and shear stresses on the solid surface. In experimental work, a force sensor is usually employed to measure the force and torque. We know that the forces exerted on a body moving through a fluid depend strongly on the local dynamic processes and flow structures generated by the body motion, such as flow separation and vortices. However, the traditional force expression cannot give us an understanding of the effects of these processes and structures on the instantaneous force characteristics. Wu and co-authors derived the DMT-based expressions [139–142] to link the vorticity field to the hydrodynamic or aerodynamic force. The advection form is introduced in the following.

For a 3D incompressible fluid domain, V_f, surrounding a solid body, B, and bounded externally by an arbitrary control surface, Σ, the theory states that

$$\boldsymbol{F} = -\rho \int_{V_f} \frac{1}{2} \frac{\mathrm{d}}{\mathrm{d}t} (\boldsymbol{x} \times \boldsymbol{\omega}) \mathrm{d}V - \rho \int_{V_f} \boldsymbol{l} \mathrm{d}V - \frac{\rho}{2} \int_{\partial V_f} \boldsymbol{x} \times (\boldsymbol{n} \times \boldsymbol{l}) \mathrm{d}S + \boldsymbol{F_B} + \boldsymbol{F_\Sigma}, \tag{34}$$

where the domain boundary, ∂V_f, includes two parts: the boundary of the control surface, Σ, and the body surface, ∂B. Here, ∂B is deformable and described by the Lagrangian variable, $\boldsymbol{x}$ is the position vector measured from an origin fixed at the model centre, $\boldsymbol{\omega}$ is the vorticity, $\boldsymbol{l} = \boldsymbol{\omega} \times \boldsymbol{u}$ is the Lamb vector, $\boldsymbol{u}$ is the velocity field, ρ is the fluid density, μ is the fluid viscosity and $\boldsymbol{n}$ is the normal unit of the domain boundary. The fourth term on the right-hand side of Eq. (34) represents the explicit contribution of body acceleration and deformation,

$$F_B = \frac{\rho}{2} \int_{\partial B} (\boldsymbol{x} \times (\boldsymbol{n} \times \boldsymbol{a_B}) \mathrm{d}S. \tag{35}$$

The last boundary integral in Eq. (34),

$$F_\Sigma = -\frac{\mu}{2} \int_\Sigma (\boldsymbol{x} \times [\boldsymbol{n} \times (\nabla \times \boldsymbol{\omega})]) \mathrm{d}S - \int_\Sigma \mu \boldsymbol{\omega} \times \boldsymbol{n} \mathrm{d}S, \tag{36}$$

expresses the viscous effect on the boundaries. Zhang et al. [94] divided the fluid domain of a swimming cownose ray into several subdomains to capture the LEV, the trailing-edge vortex (TEV) and the tip vortex (TV). By using the above expression, they gave the integration of each subdomain, i.e. the contribution of each type of vortical structure. The results showed that LEV is the main source of lift, which agrees well with that of the flying animals. However, the LEV has an unfavourable effect on thrust production. The effect of LEV on thrust attracted less attention compared with that on lift. Other parameters, such as the Strouhal number (St), as pointed out by [94], have significant effects on the role of LEV.

3.1.2 Physics and modelling of LEV

The attachment and stability of LEV at high AoA are fundamentally different from the flow phenomena in 2D or simple translating motion [20,143]. Thus, the physics and mechanisms of LEV were investigated by employing various models with theoretical [20,43,144], experimental [136,145,146] and numerical [143,147, 148] approaches. Studies utilizing different models, from simplified rectangular plates with basic kinematics [143] to realistic model of wings with complex motions [149,150], have provided different aspects of the mechanisms of LEV.

As the maintenance of the LEV is often related to the 3D effect and rotational motion, the spanwise flow within the LEV (blue arrow in Fig. 12) as well as the centrifugal (orange in Fig. 12) and Coriolis (green and purple in Fig. 12) effects due to the rotational motion is proposed by Ellington et al. [108] and Lentink and Dickinson [136] to be critical for the LEV stability. Although the mechanism of the LEV attachment and stability is still under debate, progress on the physics of LEV maintenance has been made from various perspectives in the past years. Cheng et al. [145] conducted experiments on revolving rectangular wings and visualized 3D LEV structures. They evaluated the convection, stretching and tilting of vorticity and discovered that the convection by spanwise flow is negligible compared to other effects. Wojcik and Buchholz [146] analysed vorticity transport within the LEV on a rotating rectangular plate and found that vorticity annihilation due to the interaction with the opposite-signed shear layer is important to the regulation of LEV circulation.
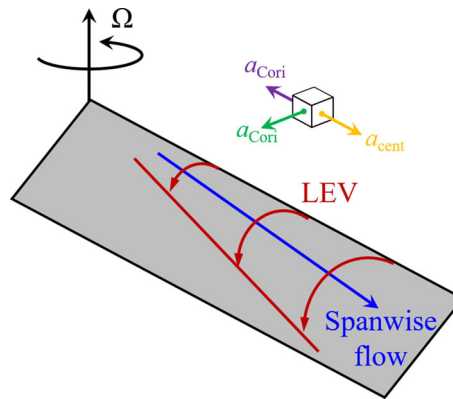
Fig. 12 Schematic of LEV on a revolving wing, where the LEV is represented by red arrows, the spanwise flow is denoted by the blue arrow, the orange arrow represents the centrifugal acceleration and the green and purple arrows denote the Coriolis acceleration due to the spanwise and streamwise flows, respectively

Limacher et al. [43] described the trajectory of an axial streamline through the LEV and found that LEV is tilted away from the leading edge under the influence of centrifugal and Coriolis accelerations. Garmann and Visbal [147] numerically investigated the dynamics of LEV on revolving wings with different aspect ratios and found that the spanwise flow induced by the centrifugal force and pressure gradient sustains the LEV, whereas the Coriolis force has no contribution to the LEV attachment. To examine the Coriolis and centrifugal effects on revolving wings, Jardin and David [148] artificially removed the Coriolis and centrifugal effects in the numerical simulation and showed that the Coriolis acceleration plays a key role in the mechanism of the LEV attachment, while the centrifugal effect has minor impact. Recently, Werner et al. [143] examined the stabilizing mechanism of the LEV on revolving wings and discovered that the gradient of Coriolis acceleration tilts the planetary vorticity into the spanwise direction, which is opposite to the LEV that limits its growth and promotes stability.

3.1.3 Forms of LEV in nature

3.1.3.1 Flapping wings with small deformation

The LEV has been applied by fliers and swimmers with different kinematical forms and in various circumstances. The most typical adopters of LEV are small flapping fliers with flexible wings, i.e. insects and hummingbird, as demonstrated in Fig. 13a. Insects and hummingbird are known for remarkable flight performance and, thus, have attracted the attention of researchers for decades. Different researches on flies [55,151], Beetles [35], cicada [103], bees [152], butterflies [153,154], hawkmoths [155] and hummingbirds [101] have shown the presence of LEV during hovering or forward flight. These fliers possess thin wings with a relatively stiff leading edge, which keeps the spanwise bending of the leading edge relatively small. Therefore, the LEV of these fliers frequently appears along the whole wingspan. On the other hand, their wings tend to passively deform during flapping flight as a result of flexibility of the thin wings. The passive deformation is considered as another important mechanism [131]. Previous studies have shown that the deformation of the wings can help in keeping the LEV attachment [151,156]. In addition, the highly manoeuvrable wing hinge of insects enables them to perform complex kinematics that optimize the lift generation. Many insects and hummingbird not only employ the LEV in the downstroke, like most fliers, but also maintain the LEV during the upstroke [55]. Thus, the lift peaks occur in both half strokes.

3.1.3.2 Morphing wings

Large flapping animals, e.g. large birds [33,132] and bats [133–135], can actively morph their wings during flight, as depicted in Fig. 13b. As the leading edge of the birds' and bats' wings experience large morphing during flight, the LEV is often attached on a partial span of the wings, e.g. hand wing in birds [33], instead of the entire span in insect flight. Moreover, unlike insects and humming bird, the lift of these large flying animals is mainly produced during the downstroke due to the difference of flapping motion [132]. Nevertheless, birds and bats are able to stabilize the attachment of LEV by actively adjusting their wings [133] or feathers [157]. Because of the high Reynolds number and complex wing kinematics, quantitative investigation of flight for large animals is challenging, and the underlying aerodynamic mechanisms have not been fully understood [7].
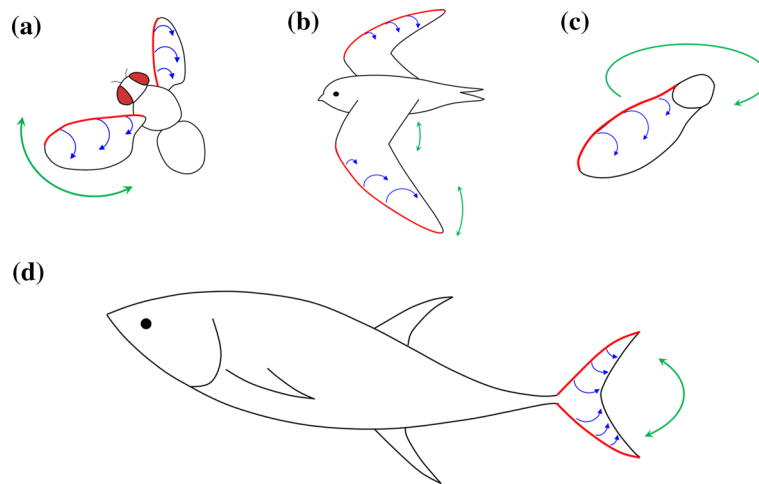
Fig. 13 Different forms of LEV in nature: **a** insect with flapping flexible wings; **b** bird with morphing wings; **c** stiff wing-like plant seed with revolving motion; **d** fish with flapping caudal fin. Red lines are the leading edge of the propulsors, blue arrows represent the LEV, and green arrows denote the motion of the propulsors

Still, progress has been made in LEV regarding large animal flight in the past few years. Videler et al. [33] conducted an experiment on the wing model of the swift and observed a stable LEV attached on the hand wing of the swift during gliding flight. Muijres et al. [133] experimentally visualized the LEV in bat forward flight and estimated that the LEV contributes more than 40% of the lift. Also, Muijres et al. [132] examined the slow flight of a passerine using PIV and found that the LEV contributes 49% of the lift, which is higher than that of hummingbirds, to compensate for the little-contribution upstroke.

3.1.3.3 Stiff revolving wings

LEV is not only employed by animals but also occurs in plants [158]. Some plants, e.g. maples shown in Fig. 13c, have evolved seeds with wing-like shape that creates lift against gravity [159]. As a result, the descent speed of these seeds is largely reduced, so the horizontal flight distance is increased under lateral wind. After falling from trees, these wing-shaped seeds start to autorotate due to their structural pattern [160]. The flow separates at the leading edge of the seeds, and the LEV is formed at the upper surface of the seeds. The LEV is stably attached during the autorotation, which significantly enhances the lift. The significant difference between the motion of the seeds and flapping flight is that the LEV is sustainably attached on the seed during the continuous autorotation, while the LEV only temporarily appears on the wings during the translational stage of flapping flight. Hence, the LEV of rotating wings has been studied through various methods [161–163]. Lentink and Dickinson [136] relate the stability of LEV to the effects of Coriolis and centrifugal accelerations. Werner et al. [143] found that vertical gradient in spanwise flow causes a vertical gradient in Coriolis acceleration, which produces the radial vorticity opposite to the LEV.

3.1.3.4 Fish and bird swimming

Although the LEV was first discovered in flapping flight, it is not exclusive to flyers in nature. Borazjani and Daghooghi [164] discovered the LEV attached on the caudal fin in fish-like swimming. By examining models with different caudal fin shapes, they found that the attachment of the LEV is due to the fish-like kinematics instead of the delta shape of the fin. Later, the LEV was gradually observed in fish swimming numerically [87,120,121] and experimentally [165]. Besides fish swimming, the LEV was also found in the propulsion of swimming birds with webbed feet. Johansson and Norberg [137] conducted experiments on foot model with motion mimicking the diving cormorant and discovered the LEV on the suction side of the foot.

3.2 Trailing-edge vortex (TEV)

3.2.1 Starting motion by an analytical model

Firstly, we try to explain the physics of trailing-edge vortex (TEV) of a starting motion using an analytical model. For the starting motion, the starting vortex is referred to as the TEV. The form of the starting vortex
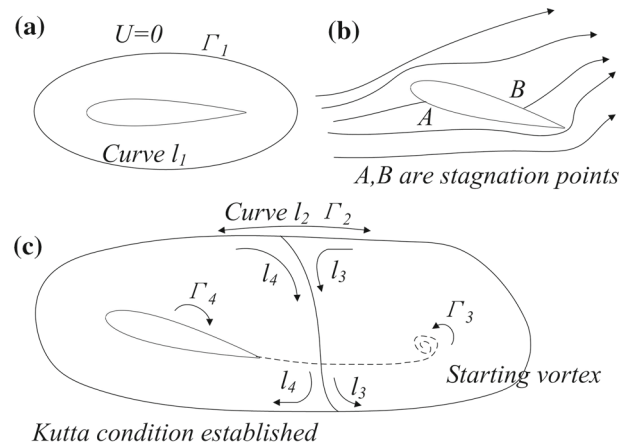
Fig. 14 Schematics of the starting vortex forming process: **a** aerofoil at rest; **b** streamlines on starting before the establishment of the Kutta condition; **c** when the Kutta condition is satisfied, a bound circulation is formed as well as a starting vortex with opposite circulation

generated when a flat-plate airfoil is accelerated from rest has attracted much attention. Previous studies [166–168] have shown that the flow structures of impulsively started translating and revolving wings are similar and so are the unsteady force histories. Thus, although a number of features of insect flight are omitted, the study on an impulsively started translating wing can provide a deep understanding of TEV.

Consider that the airfoil is starting to move from rest (Fig. 14a). At start, before the Kutta condition has been established, one would expect the fluid to deflect due to the presence of the airfoil, generating a flow field around the wing similar to that shown in Fig. 14b. Under such conditions, the rear stagnation point (where velocity is zero) would be present not at the tip of the trailing edge but on the upper surface of the foil, i.e. the flow at the lower surface must bypass the sharp trailing edge to meet the flow at the upper surface. Such a flow profile generates high-velocity gradients at the trailing edge, thereby causing high levels of vorticity. The high vorticity then moves downstream as it moves away from the trailing edge. As they move away, this thin sheet of intense vorticity is unstable and consequently tends to roll up to give a point vortex, which is called the starting vortex. As shown in Fig. 14c, this starting vortex has a counterclockwise circulation. According to the Kelvin's circulation theorem, at the shedding of the starting vortex (with a circulation of Γ_3), an equal-and-opposite clockwise circulation, Γ_4, is generated around the airfoil, which is called the bound circulation. The lift generated by a wing is related to the amount of bound circulation.

As the starting process continues, vorticity from the trailing edge is constantly fed into the starting vortex, making it stronger. In turn, the circulation Γ_4 around the airfoil becomes stronger, making the flow at the stagnation point more closely approach the trailing edge. Finally, the starting vortex grows up to just the right strength such that the opposite clockwise circulation around the airfoil causes the fluid to smoothly leave the trailing edge (the Kutta condition is exactly established). At that moment, the vorticity of the shed vortex becomes zero and a steady circulation exists around the airfoil. Under steady-state conditions, the bound circulation is formed due to the shedding of the starting vortex, but in cases with unsteady aerodynamics, the circulation around the wing also includes the LEV circulation.

3.2.2 LEV-inspired TEV

Unlike the conventional fixed-wing aircraft, natural flyers flap their wings at a high AOA without stall. For such an unsteady case in viscous fluid, e.g. a harmonic oscillating airfoil or a large-angle translation, flow will firstly separate at the leading edge and the formation of TEV is always affected by the formation of LEV. In this section, we will introduce two types of LEV-inspired TEV, as shown in Fig. 15. The first type of TEV is developed with the interaction of the lower part of the detached LEV; then, it sheds downstream together with the LEV (Fig. 15a). For the second type, the LEV is combined into the corotating TEVs and then sheds downstream (Fig. 15b), which is called synchronized shedding type by Ohmi et al. [169]. In the following, we give some examples of these two types of TEV formation.

Panda and Zaman [170] visualized the wake flow of an airfoil pitched sinusoidally with an AOA in the range of 5° to 25°, as shown in Fig. 16. Figures 16a–f show the upstroke phases, and Figs. 16g–j show those
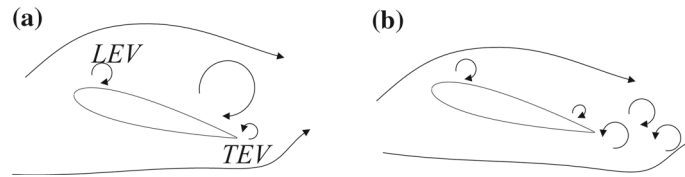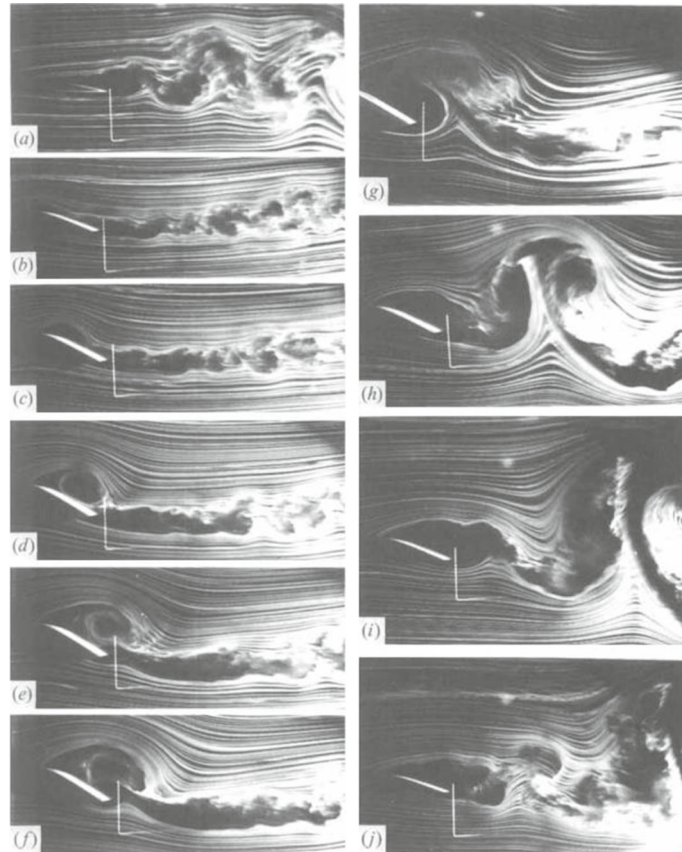
Fig. 15 Two types of LEV-inspired TEV

Fig. 16 Smoke-wire flow-visualization photographs at different phases of a pitching foil, showing the formation of TEV. Adapted with permission from [170]

of the downstroke. As the AOA increases, a clockwise vortex (LEV) forms on the airfoil surface (Fig. 16d). With further increase in the angle, the LEV moves towards the trailing edge. When it reaches the trailing edge, the associated low pressure due to the presence of LEV rapidly pulls fluid with anticlockwise vorticity from the pressure surface, causing the formation of the TEV (Fig. 16f). Then, the TEV grows quickly beneath the LEV (Fig. 16f, g) and combines with the latter to form a mushroom-like structure, which evolves and convects downstream.

The vortex evolution of a swimming cownose ray [94] is presented in Fig. 17 to show the synchronized shedding type. At the early upstroke, a shear layer is formed at the leading edge (Fig. 17a). The LEV begins to form at the mid-upstroke (Fig. 17b), and then, it breaks (Fig. 17c), merges into the shear layer (Figs. 17d, e) and finally sheds in the form of TEV (Fig. 17f). Such TEV formation can also be found in tuna [164] and bat [133].

3.2.3 Fast-pitching motion

Some hovering animals use a distinct mechanism to generate TEV. Mosquitoes exhibit remarkably high frequencies and low stroke amplitudes [171]. Early in the downstroke, although the trailing edge has a very low
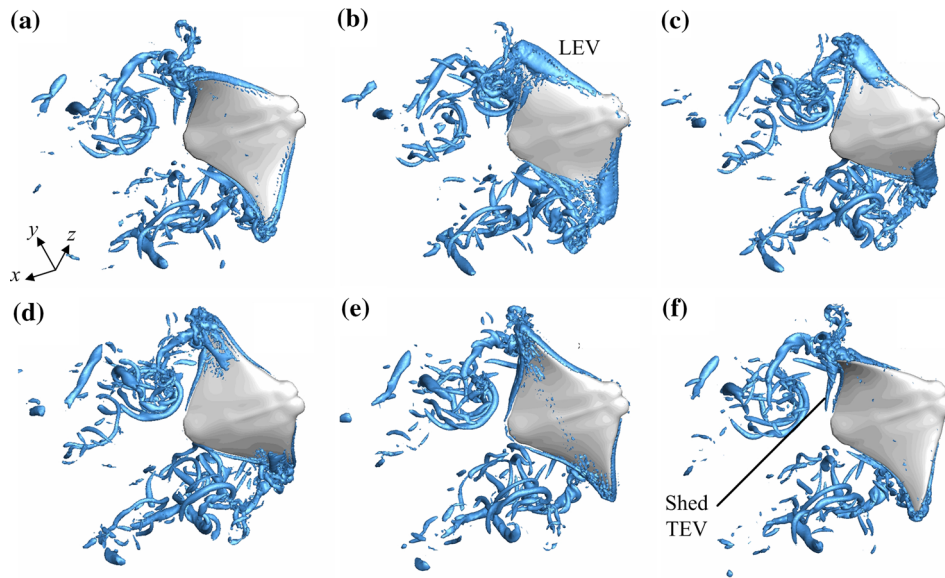
Fig. 17 The vortex evolution of a swimming cownose ray. Reproduced with permission from [94]

ground speed, there exists a high-speed flow induced by the preceding upstroke which encounters the trailing edge at a high AOA. Under the influence of such flow, the flow speed and pressure gradient are sufficient for the shear layer to roll up into a coherent TEV. With a small stroke amplitude, the wing of a hovering hoverfly [172] travels only a short distance. However, the wing moves rapidly downward and forward at a large AOA during a short period, leading to the formation of TEV.

3.2.4 Role of TEV on force production

Given the mechanisms of the formation of the TEV, the effect of the TEV on force has attracted less attention compared with that of the LEV. Regarding the role of the TEV on lift production, Bomphrey et al. [171] provided an evidence that the first peak in the lift force of free-flying mosquitoes early in the downstroke is due to the attachment of the TEV. Also, Zhang et al. [156] gave a quantitative analysis of the contribution of the TEV using the DMT-based force expression. In their computation, the TEV makes more significant contribution to lift than the LEV. Zhu [172] and Liu et al. [56] found different lift enhancement mechanisms of the TEV in different insects. They used the time rate of change in the total first moment of vorticity in the fluid to measure the force production. For most insects, such as dragonfly, in which the LEV mechanism dominates the lift production, the vorticity in the LEV does not change greatly with time as the LEV is attached to the model surface. A high rate of change in the first moment of vorticity, i.e. a large lift, is due to an increase in the distance between the LEV and the starting vortex, because the LEV moves with the wing motion and the wing travels a long distance. For hoverflies and mosquitoes, the distance between the two vortices changes slightly, and a fast change in vorticity moment is produced by a rapid generation and increase of the opposite vorticity at the trailing edge.

However, regarding thrust production, as mentioned above, the contribution of TEV is found to be unfavourable [94] to the thrust production of batoid fish swimming, using a similar DMT-based force expression.

3.3 Tip vortex (TV)

3.3.1 Stationary wings

The tip vortex (TV) associated with stationary finite wings is a common phenomenon. Without the obstruction of wing surface at the wing tip, the flow on the lower surface bypasses the wing tip and flows to the upper surface. Such flow and the incoming flow are superimposed to form a spiral flow, which forms the wing-tip

vortex. For stationary wings, the TV is typically the dominant vortical structure. The TV completes its roll up within one chord length downstream of the trailing edge, and the circulation of TV remains nearly constant up to $x/c = 6$. The velocity distribution and the overall circulation were found to be directly influenced by the Reynolds number and the incidence angle [173]. The TV of a stationary wing will causes many problems, such as wake encounter [174], induced drag [175] and aerodynamic noise [176]. Investigations of the TV behind a stationary wing can be found in [174,177,178].

3.3.2 Dynamics of TV

In order to reduce the influence of the spanwise variation in kinematics and model shape, flat plates and flapping wings are the most widely used model to study the physics of TV. Among the representative TV investigations, the first main conclusion is that it influences the distribution of LEV. The circulation of LEV was found to decrease at spanwise positions close to the tip [179]. On the one hand, this is because the effective AOA is reduced by a downwash effect of the TV, and thus, it produces less spanwise vorticity. On the other hand, the spanwise vorticity (LEV) near the tip tilts itself to align with the streamwise vorticity (TV) [180], as shown in Fig. 18a. The tilting vortex induces a spanwise flow, and the strength of such spanwise flow influences the motion of TV reversely.

For a small aspect-ratio rotating plate, the aft-tilted LEV is merged with the TV [181,182]. The TV of a small aspect-ratio translating plate (Fig. 18b) was found to move more inward than a rotating one (Fig. 18c) [180]. For attached-flow and light-stall pitching foils (oscillations within and through the static-stall angle), many of the vortex flow features are qualitatively similar to the TV behind a static wing, except that they produce a less concentrated vortex of similar diameter and have a larger radial gradient in circulation strength [183]. For deep-stall pitching foils (oscillations beyond the static-stall angle), a strong distinction in contour shape and magnitude between the pitch-up and pitch-down phases during the pitch cycle is observed, including the axisymmetry, tangential velocity and vortex size. This difference is primarily because during pitch-up, the boundary layer remains attached to the surface of the wing, whereas during pitch-down, the flow is largely separated.

TV has a more complex structure than that often reported in literature. Li et al. [184] reported a paired TVs around rotating wings at the front and bottom corner of the wing tip, respectively, at higher aspect ratio ($AR > 1$) or higher AOA ($\alpha > 30°$). The secondary TV is produced from the TEV and the vortex structure is quite robust even for different wing geometries. Similar structures were also observed in fruit fly wings [185].

From the above-mentioned studies, it is evident that a strong vortex interaction influences vortex formation and growth. By neglecting the diffusion term in the vorticity transport equation, Hartloper et al. [186] used the z-vorticity transport equation to describe the vortex dynamics:

$$\frac{\partial \omega_z}{\partial t} + u\frac{\partial \omega_z}{\partial x} + v\frac{\partial \omega_z}{\partial y} + w\frac{\partial \omega_z}{\partial z} = \omega_x\frac{\partial w}{\partial x} + \omega_y\frac{\partial w}{\partial y} + \omega_z\frac{\partial w}{\partial z}, \tag{37}$$

where the left-hand terms represent the local unsteady change in vorticity and vortex convection, respectively, while the right-hand terms represent x-tilting (streamwise), y-tilting and z-stretching (spanwise), respectively. At the beginning of the pitching motion for a low-aspect-ratio plate, the x- and y-convective terms dominate. Afterwards, the x- and y-tilting terms are increased dramatically, indicating that there is an increased interaction between the LEV and TV. Physically, the presence of the x- and y-tilting in the z-vorticity transport equation means that the z-vorticity from the leading-edge vortex is reoriented into the x- and y-vorticity of the TV [180]
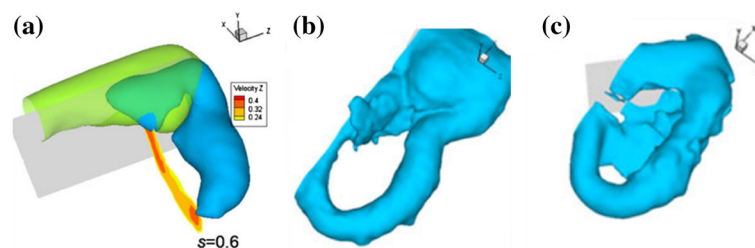

Fig. 18 a Iso-surfaces of spanwise vorticity (transparent green), streamwise vorticity (blue) and a contour of spanwise velocity on the xy-plane. Vortex structure by a **b** translating plate and **c** rotating plate, which are visualized by the iso-surfaces of vorticity magnitude. Reproduced with permission from [180]
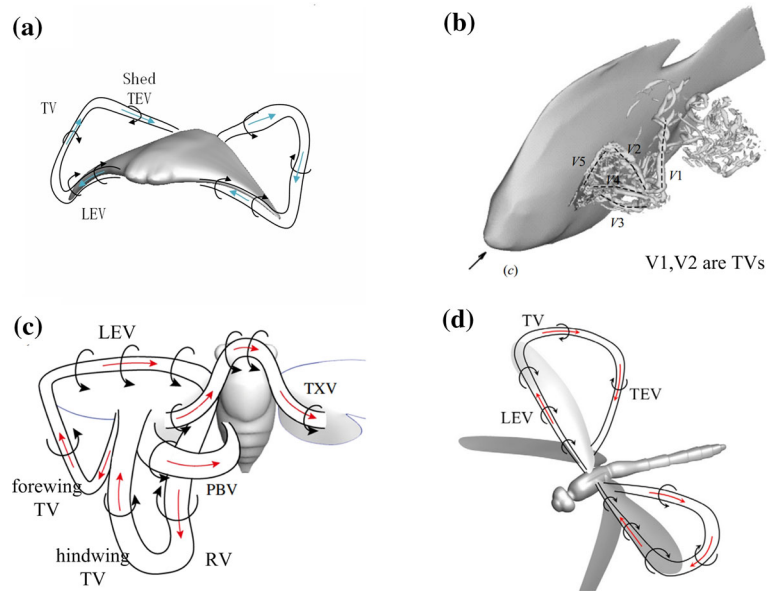
Fig. 19 Schematics of the wake structures of **a** cownose ray, **b** bluegill sunfish, **c** cicada and **d** dragonfly. Adapted with permission from [94,105,188,189]

(Fig. 18a). Some studies present the phenomenon of LEV eruption [180,186,187] (Fig. 18b), which is because of the spanwise compression of z-vorticity. From the transport equation, a negative z-stretching indicates the spanwise compression of z-vorticity at inboard regions on the plate.

3.3.3 TVs in swimming and flying animals

For natural animals, the TV is highly unsteady and periodic. Spanwise flow can accelerate the formation of wing TVs and then interact with the latter. Moreover, TVs and wake vortices always form closed loops [37,55,56,94,103,105,188,189]. As shown in Figs. 17 and 19a, the LEV, shed TEV and TV of the cownose ray form a closed loop. For the pectoral fin of a bluegill sunfish (Fig. 19b) moving primarily in the anteroposterior direction, the adduction TV (V2), shed ventral and dorsal LEV (V3 and V4) and the attached LEV (V5) form a closed loop. V3 and V4 are formed during the early stage of adduction, whereas V5 is formed during the later stages of adduction. The cicada has more complex wakes (Fig. 19c), which has two TVs, formed at the forewing and hindwing, respectively. Moreover, there are two unique vortical structures formed at the thorax and posterior body, i.e. the thorax vortex (TXV) and posterior body vortex (PBV). TXV and PBV interact with the root vortex. These identifiable vortex structures form a closed dual loop. The closed loop of a turning dragonfly's forewing (Fig. 19d) is similar to that of a cownose ray. Note that the hindwing also forms a similar vortex loop, which interacts with the former.

3.3.4 Role of TV on force generation

Although the region of wings or fins covered by the TV is a small area, its contribution to force generation needs more attention. To investigate the role of TV, it is important to isolate the tip effect from the vortex dynamics because the formation of TV is always accompanied by a strong vortex interaction as stated above. Among the limited investigations, it is generally considered that the TV is beneficial to force generation in some circumstances.

Ringuette et al. [179] considered low-AR flat plates of rectangular planform with a free end and a grazing end condition, respectively. For the grazing end, they placed a raised bottom wall less than 1 mm below the plate's free end to suppress the flow around the tip. Their results showed that the interaction between the TV and LEV generates more than 46% drag, whereas suppressing the flow around the tip results in significantly lower drag. Moreover, a relatively larger tip effect can be achieved by a smaller aspect ratio.

Shyy et al. [190] investigated the role of TV by comparing the 3D flapping wing and that of 2D, which has no TV. The lift histories and the lift per unit span are shown in Fig. 20, which presents different roles for
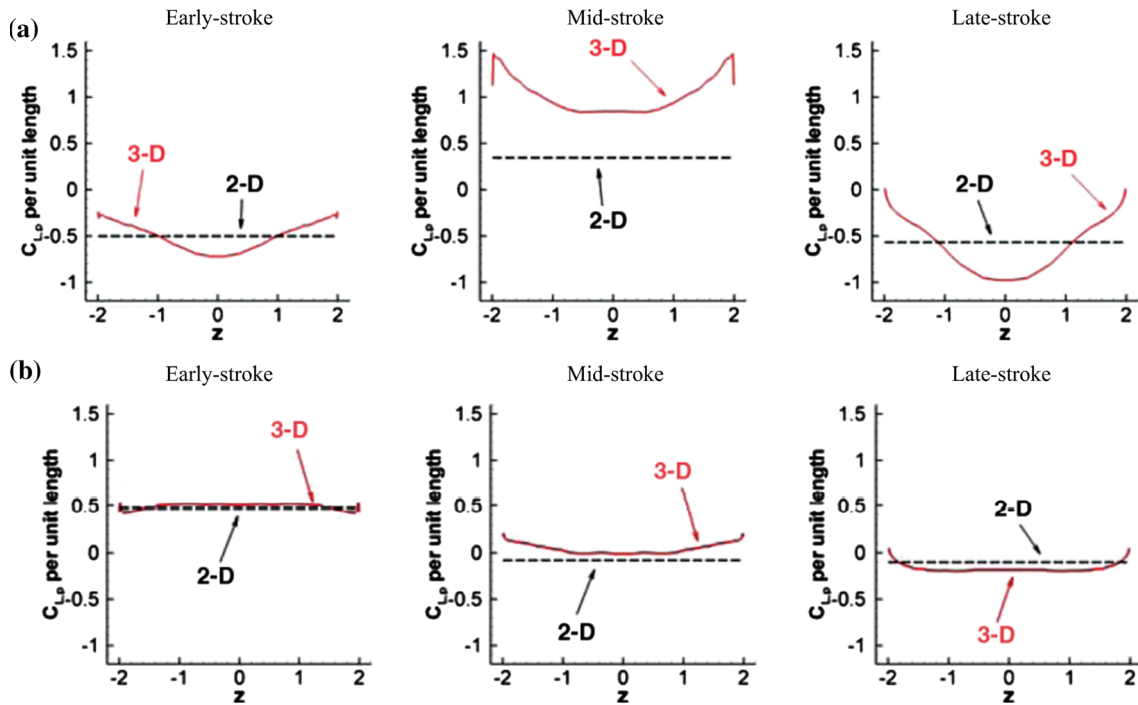
Fig. 20 The lift per unit span snapshots of the wing at the selected time instants versus the 2D equivalent, **a** with a delayed rotation, i.e. the pitching motion lags that of the plunging motion and **b** without phase lag. Z is the spanwise direction, and the locations of $Z = \pm 2$ represent the tip region. Adapted with permission from [190]

various kinematics. In Fig. 20a, it is evident that the TV can enhance the lift for the majority of the stroke cycle. The lift enhancement is due to both the low-pressure region created by TV and the anchoring of LEV to delay or even prevent shedding by the tip flow. Note that the above flapping wing employs a combined translational and rotational motion with a plunging amplitude of twice the chord length, an angular amplitude of 45° and a phase lag between translation and rotation of 60°. However, by varying the kinematics, a distinct role of TV can be disclosed, as shown in Fig. 20b. For a synchronized motion with no phase lag, where the LEV remains attached along the spanwise direction, the differences between the 2D and 3D simulations are small, and the effect of TV is not prominent. Regarding natural animals, the role of TV for the cownose rays was revealed by Zhang et al. [94]. The method to isolate the tip effect is the same as that used in the investigations of LEV and TEV. A new TV mechanism for thrust force enhancement was found in MPF oscillatory swimming. At high Strouhal number condition, it was found that the TV plays a vital role in the cownose ray thrust generation. For a larger chordwise deformation, a weaker TV is produced, and thus, the contribution of TV is relatively smaller. However, at low St, the contribution of TV is decreased significantly because the ω_z structures transform from the tip domain to the LEV domain, and the contribution to thrust was found to be related to the vorticity distribution.

3.4 Vortex interaction

Moving bodies within viscous fluid generate vortices, which play a crucial role in organizing flow. The vortices, in turn, have a significant influence on the body in the fluid. Flyers and swimmers in nature are thought to be able to actively or passively take advantage of the interaction with the vortices to save energy or enhance locomotor performance. Bird flocks in V-formation and fish schools (illustrated in Fig. 21a, b) are famous examples that individuals benefit from vortex interactions. These collective behaviours have long drawn researchers' attention for decades [191]. One of the early foundational works on the V-shape formation of birds is the analysis by Lissaman and Shollenberger [192]. They showed that the birds in a V-formation benefit from the upwash induced by the wing-tip vortices of the preceding birds. For fish schools, the calculations of Weihs [193] indicated that fish swimming in a diamond-shaped lattice arrangement enables individuals to save energy due to the flow induced by the vortices shed from the upstream fish. This beneficial vortex interaction is not
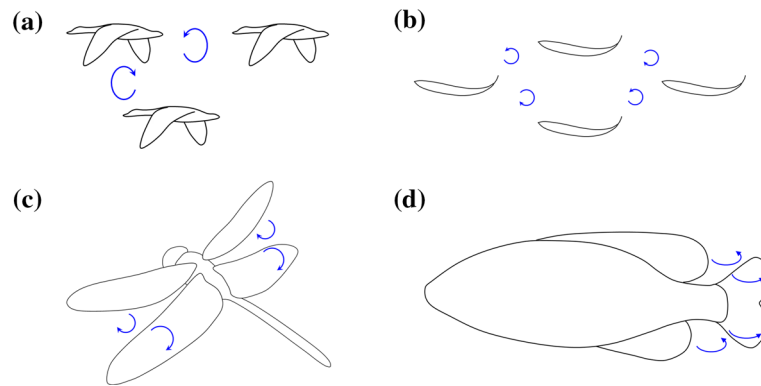
Fig. 21 Illustration of vortices interactions in nature: **a** V-formation birds flock; **b** fish schooling; **c** interaction of wings in insect flight; **d** vortices interaction of fins in fish swimming, where the blue arrows represent the vortices
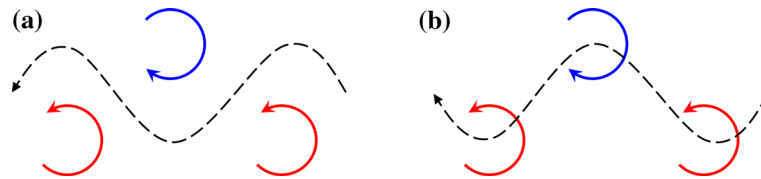

Fig. 22 Schematics of the slalom mode (**a**) and the interception mode (**b**). The red and blue circle denotes the vortices shed from the upstream flag, and the dashed line represents the trajectory of the downstream flag

restricted to multiple individuals but also occurs in a single individual, e.g. interaction of the forewing and hindwing in the flight of dragonfly [194,195] (Fig. 21c) and interaction between the dorsal and caudal fins in swimming fish [121,196] (Fig. 21d). The board forms of vortex interaction lead to numerous studies on various subjects, from tandem filaments [197] to free-flying birds [198], through different methods, including theoretical analysis [199,200], experiments [201,202] and numerical simulations [41,203].

3.4.1 Interaction of flapping foils

As concluded above in Sect. 2, the propulsors (wings or fins) of flapping-based flying and swimming can be modelled as foils undergoing flapping motion. Thus, simplified models consisting of multiple foils [191,201, 203], plates [204,205] or filaments [206–208] are widely applied to study vortex interactions in biomimetic propulsion. These approaches extract key component from the complexity of biological flying and swimming without loss of generality and enable precise control and measurement of numerous variables to gain insight into the fundamental mechanisms of vortex interaction. Tremendous progress has been made in vortex interactions owing to the system of flapping foils.

As the vortex interaction exists in different forms, studies on diverse models have been conducted. Many animals can react to upstream vortices, whether it is shed from another individual or not. Thus, several studies focused on the interaction of a simplified body with environmental vortices, e.g. the von Kármán vortex street. Streitlien et al. [209] theoretically analysed the inviscid model of a 2D heaving and pitching foil in the von Kármán vortex street represented by point vortices. It is shown that foil can exploit the energy in the vortex street and the efficiency is largely increased. By varying different parameters, they also found that the phase between the foil motion and the arrival of upstream vortices is critical, and the highest performance is achieved when the foil moves close to the incoming vortices. Alben [210] proposed a theoretical model for swimming of a flexible body in a vortex street and discussed optimal swimming motions for simplified problems. Using soap film tunnels, Jia and Yin [207] conducted an experiment on a flexible filament in the wake of a cylinder. They found that the filaments exhibit phase lock-in by the wake of cylinder and show three interaction modes, distinguished by the net streamwise force, at difference distances between the filament and the cylinder. Recently, Wang et al. [211] numerically investigated self-propelled plate in the wake of two tandem cylinders. Three locomotion modes of the plate, namely drifting upstream, downstream and holding stationary, were identified depending on the initial position.

As a minimal unit, two-body system was utilized by many studies to investigate vortex interaction between wings and fins in flying and swimming. Maybury and Lehmann [212] employed two dragonfly-like plates to experimentally investigate the interaction of the forewing and hindwing in dragonfly hovering flight. By changing the phase difference between the wings, it was shown that the lift of the hindwing varies, while the performance of the forewing has no major difference. They proposed that the change in strength of the LEV, introduced in Sect. 3.1, on the hindwing due to the interaction with the forewing is responsible for the variation of lift. Wang and Russell [213] numerically investigated the forewing and hindwing interaction in dragonfly using 2D flapping plates. They discovered that the out-of-phase motion minimizes the power consumption to generate the lift to balance the weight, and the in-phase motion contributes additional force to acceleration. Xie and Huang [214] further examined the interaction of dragonfly wings using tandem flapping plates. By varying the phase difference and the distance between the two wings, two vortex interaction modes were identified corresponding to the enhancement of the lift forces of the forewing and hindwing, respectively. Akhtar et al. [204] simulated heaving and pitching tandem plates to study the interaction between the dorsal and caudal fins in sunfish. They found that vortices shed from the upstream plate enhance the LEV of the downstream plate and, thus, increase the thrust of the caudal fin. Ristroph and Zhang [215] experimentally investigated the tandem flags in a flowing soap film and discovered the inverted drafting phenomenon, where the downstream flag suffers a drag increase. Jia and Yin [206] also used flexible filaments in a flowing soap film to observe the interaction in a tandem system and found that the downstream filament extracts energy from the vortex shed from the upstream filament and produces greater force. Alben [216] and Kim et al. [217] examined two tandem flexible flags and found that the constructive and destructive modes of the vortex interaction were affected by the gap distances and the bending coefficient. Boschitsch et al. [218] conducted experiments using two in-line pitching foils over wide foil spacing and phase differential ranges. The downstream foil performance was closely related to the phase differential and spacing between the foils. Uddin et al. [42] simulated tandem flapping flexible flags and identified two interaction modes, the slalom and interception modes, corresponding to the low drag and high drag statuses, respectively. In the slalom mode (Fig. 22a), the direction of the downstream flag coincides with the vortex-induced velocity, whereas the flow induced by the vortices in the interception mode (Fig. 22b) resists the downstream flag. Kurt and Moored [219] experimentally investigated the interaction of two pitching plates in an in-line configuration under 2D and 3D conditions. Two interaction modes distinguished as the coherent and branched interaction modes were identified, which were not directly related to the propulsive efficiency. A parametric study was also performed to explore the optimal conditions of thrust and efficiency. Recently, Newbolt et al. [191] systematically studied the interaction of two tandem flapping hydrofoils and discovered that the posterior hydrofoil cohesively follows the anterior one due to the wake interaction.

Some other studies explored interaction systems containing more than two bodies. Uddin et al. [41] numerically investigated the interaction of multiple flexible flags in triangular, diamond and conical formations containing three, four and six flags, respectively. By adjusting the streamwise and spanwise gap distances and the flag bending coefficient, single-frequency and multifrequency modes were identified, which generally correspond to the constructive and destructive interaction modes in a two-body system exhibiting higher and lower drag, respectively. Han et al. [220] employed three tandem pitching foils to represent a fish possessing two dorsal fins. Compared with the two-foil system, they found that the three-foil system enhances the thrust and efficiency more significantly at the optimal condition. Peng et al. [221] numerically investigated the interaction of multiple self-propelled flexible plates in tandem arrangement. Two schooling modes, fast mode with compact configurations and slow mode with sparse configurations, were observed due to the flow-mediated interactions among the individual plates. Recently, Lin et al. [222] simulated multiple self-propelling flapping foils and found that the multiple foils spontaneously organize a compact formation, where all of them move like an anguilliform swimmer, through hydrodynamic interactions. The anguilliform-like formation of foils increases velocity, decreases energy consumption of each foil, and can be self-organized over a wide range of conditions.

3.4.2 Interaction of complex bodies

Although the interaction of flapping foils has been well studied, vortex interaction in real animal propulsion may exhibit different traits considering various complex effects. Therefore, studies on living animals or highly realistic models have also been performed to reveal the underlying mechanisms of vortex interactions in animal flying and swimming. Bode-Oke et al. [106] simulated the backward flight of a dragonfly using a model reconstructed from measurement data. By comparing with the model without forewings, they found
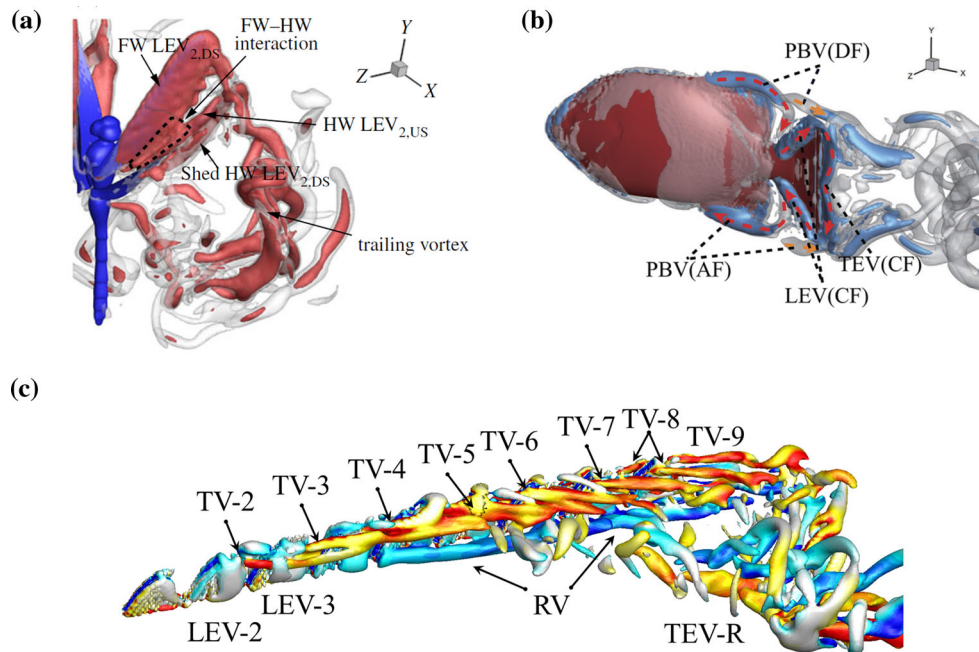
Fig. 23 3D visualizations of vortex interactions of complex bodies: **a** interaction of forewing (FW) and hindwing (HW) of dragonfly [106]; **b** interaction of posterior body vortices (PBV), shed from dorsal fin (DF) and anal fin (AF), and LEV of caudal fin (CF) [121]; **c** interaction of LEVS, TVs, TEVs and root vortices (RVs) of tuna finlets [223]

that vortices shed from the forewing enhance the LEV on the hindwing (Fig. 23a) and, thus, increase the force production. Analogously, enhancement of the aerodynamic performance of hindwings was also found in damselfly due to the vortex interaction with the forewings [37]. Liao et al. [224] conducted an experiment on trout in a von Kármán street produced by a D-cylinder and found that the trout maintained the streamwise position by gliding between the vortices. A further energetic study [225] directly confirmed that the energy consumption of a swimming fish is reduced by interacting with environmental vortices during swimming in a vortex street. Drucker and Lauder [226] measured the functions of a dorsal fin in sunfish by digital particle image velocimetry (PIV) and found that wakes shed from the dorsal fin enhance the vortices around the caudal fin. Zhu et al. [49] numerically explored vortex interaction between the dorsal fins and caudal fin in fish-like models and identified two distinct interaction modes that result in high and low thrust, respectively. The interaction of fins in trout was explored through experiments [227,228] showing that rather than encountering free-stream flow, the caudal fin undulates through the incident flow altered by the wakes of dorsal and anal fins. Liu et al. [120] numerically addressed the vortex interactions of the body, dorsal fin and caudal fin of jack fish. They showed that the LEV attached to the caudal fin is enhanced by capturing vortices shed from the body, a process known as the caudal fin wake capture mechanism. Recently, Han et al. [121] examined median–fin interactions (dorsal, anal, and caudal fins) by simulating sunfish models with experimental kinematic data. By comparing the wake structures of models with different dorsal fin sizes, they found that the thrust and efficiency of the caudal fin are substantially improved by the LEV of the caudal fin strengthened by the vortices shed from the posterior body and the dorsal fin, as shown in Fig. 23b. Wang et al. [229] numerically investigated the hydrodynamic interaction of tuna finlets using kinematic data from measurement of a free-swimming tuna. They discovered that the vortex interaction among the finlets reduces drag and the pitching motion of the finlets decreases the power consumption. Zhang and Huang [223] further established a symmetric kinematic model of tuna finlets and specifically examined the effect of the first two and the last two finlets. They found that the first two finlets significantly decrease the drag of the third and fourth finlets due to the vortex interaction (Fig. 23c) and slightly reduce the drag of the other posterior finlets.
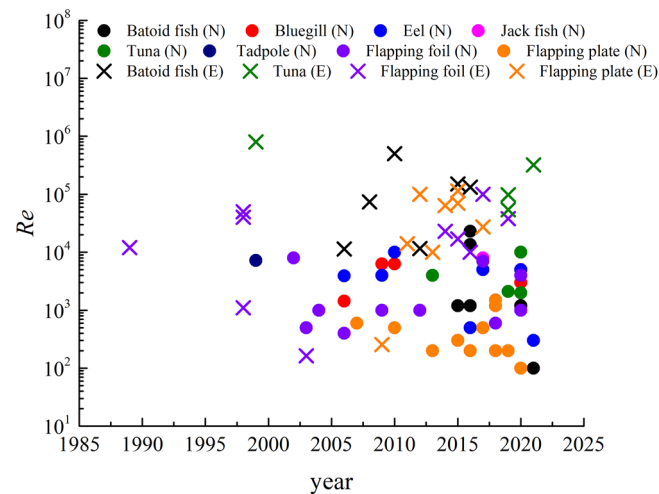
Fig. 24 The Reynolds numbers used in recent works of batoid fish [51,95–97,123,232–237], bluegill [100,121,188,238], eel [48,79,83,122,239–242], jack fish [120,243], tuna [87,164,229,244–247], tadpole [248], flapping foil [93,204,249–263] and flapping plate [59,63,70,264–278]; the circle represents high-fidelity numerical work (labelled by N) and the fork represents experimental work (labelled by E)

3.5 Reynolds number effect

Various species of animals and even a single species at different stages swim/fly in a wide range of Reynolds numbers (Re). For example, from small amphibians, like tadpoles, to large mammals, like dolphins and blue whales, the Reynolds number (Re) spans seven orders of magnitude [230]. In the complete life cycle of zebrafish, from larvae to adult, Re ranges from 10 to 10^4 [231]. Moreover, achieving high Reynolds numbers in a laboratory or numerical environment for swimming/flying is challenging. We summarized the Reynolds numbers in some works of swimming animals and flapping foils in recent decades, as shown in Fig. 24. Experimental work can reach a relatively high Reynolds number but far from large swimming animals. High-fidelity numerical works were mostly below Re of 10^4 because high-Re simulation brings many challenges. For the above reasons, the Reynolds number effect on the propulsion mechanisms needs to be well understood.

3.5.1 Effect of Re on vortex dynamics

The most intuitive effect is that viscous diffusion at low Reynolds numbers will remove small structures. For the swimming of larvae ($Re = 10 - 10^3$) and adult ($Re = 10^3 - 10^4$) zebrafish, vortex rings are stable and not likely to break up at Reynolds numbers below 10^4 [279], while viscous diffusion removes all traces of wakes within less than 0.5s of the wake being shed. Bozkurttas et al. [100] investigated the flow of a highly deformable fish pectoral fin at a small range of Reynolds numbers ($540 - 6300$). The results showed that as the Reynolds number decreases, the structures get simpler and the helical structure of the abduction tip vortex becomes less noticeable; however, it does not change the similarity in the vortex topology.

Also, the Reynolds number affects the vorticity generation on the surface of the body. Usually, low-Re swimmers/fliers have a much thicker boundary layer relative to their body size [45]. Kim and Gharib [180] indicated that a small-aspect-ratio rotating plate does not form a starting vortex at $Re = 60$ as distinctly as that of $Re = 8800$. Moreover, TVs are more widely distributed for the low-Re case, leading to a stronger spanwise flow over the rear area of the plate. Jantzen et al. [280] compared the vortices for a large-aspect-ratio pitching plate at $Re = 300$ and 20,000. The LEV core for the low Reynolds number case is elongated, whereas for the high Reynolds number case, it is more compact towards the leading edge. Such difference creates a distinction in the suction region, resulting in different lift forces. At high Reynolds numbers, the vortices at the trailing edge are more broken into a series of eddies due to the appearance of the Kelvin–Helmholtz instability.

Another effect of Re is vortex stability. Shyy and Liu [281] compared the vortical structures of flying insects at three Reynolds numbers, i.e. $Re = 10, 120, 6000$, as shown in Fig. 25. At $Re = 6000$ (Fig. 25a), an intense, conical LEV was observed to break down at approximately three quarters of the span towards the tip, whereas at $Re = 120$ and 10 (Fig. 25b, c), the LEV no longer breaks down and is connected to the TV.
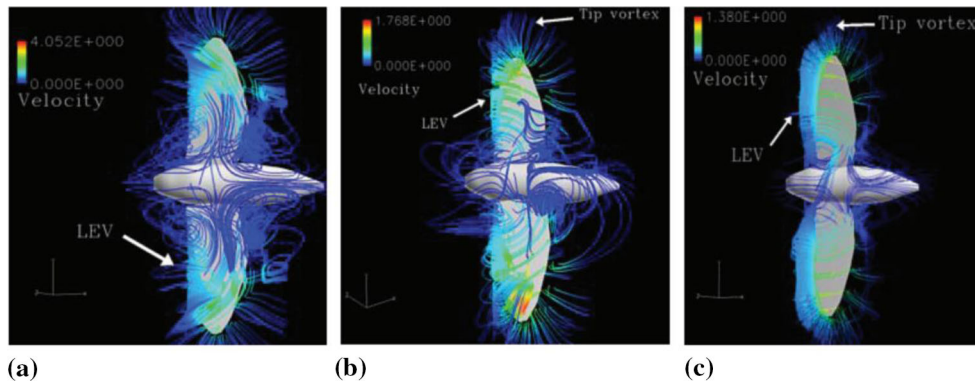
Fig. 25 Numerical results of vortex structures at Reynolds numbers of **a** $Re = 6000$ **b** $Re = 120$ and **c** $Re = 10$. Adapted with permission from [281]
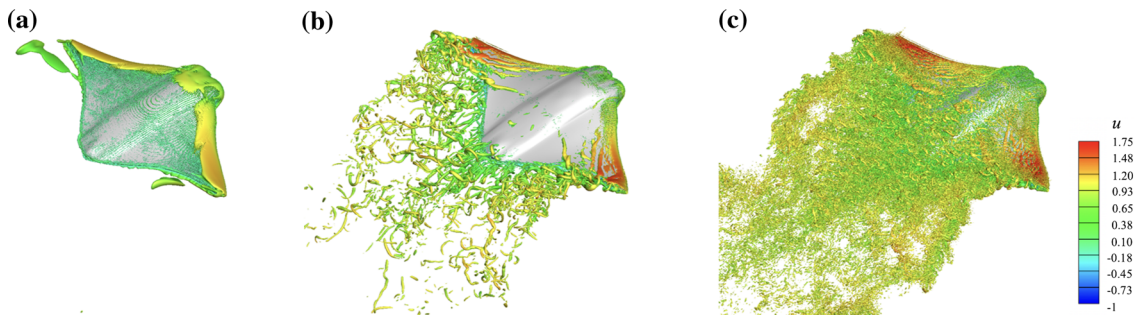

Fig. 26 Instantaneous vortex structures around a cownose ray visualized by the iso-surface of $Q = 300$ at **a** $Re = 1480$, **b** $Re = 14800$ and **c** $Re = 148,000$

The spanwise flow at the vortex core is also observed to become weaker with a decrease of Reynolds number. In some cases, the LEV breaks into dual vortex structures [282,283] with increasing Reynolds number, which is accompanied by the development of an opposite-sign vorticity layer and the formation of a secondary counterrotating vortex [146]. Lentink and Dickinson [136] found that the LEV on a revolving fly wing exhibits spiral bursting beyond $Re = 1400$; however, the LEV-based force augmentation is robust in the Re range of 110 to 14000. On translating wings, vortex bursting was not observed, while more erratic flow after a tight vortex was formed and separated from the wing, suggesting a transition to turbulent flow. To see more clearly, we conducted high-fidelity simulations of cownose swimming at different Reynolds numbers, as shown in Fig. 26. The morphological and kinematic model is obtained from [94]. A hybrid immersed boundary/wall-model approach for large eddy simulation [284,285] was employed to simulate the high-Reynolds-number turbulent flow. At $Re = 14800$ (Fig. 26b) and $Re = 148,000$ (Fig. 26c), the LEV detaches from the boundary and then reattaches at the two-thirds body length position. In contrast, at $Re = 1480$ (Fig. 26a), a thicker boundary layer is formed and the reattachment does not occur. The transition from laminar to turbulent flow can be easily captured with the increase of the Reynolds number.

3.5.2 Effect of Re on forces

At low Re, viscous forces dominate the flow for small and slow animals, whereas inertial forces dominate the flow for large and fast animals at high Re. The thrust coefficient and the efficiency display a strong Reynolds number dependence, as shown in Fig. 27. Increasing Re tends to increase the force production (Fig. 27a) and efficiency (Fig. 27b), but decrease the drag. For free swimming/flying models, increasing Re means increasing the swimming/flying speeds and efficiency [45]. A similar trend can be found in the studies of natural animals [87,100,120,156,283]. For instance, the efficiency of a crevalle jack is 16% at Re = 2100, while it increases to 21.7% at Re = 8000 [120]. Note that the effect of Re is limited. The increment of the eel's speed and efficiency is asymptotic beyond the Re of 5×10^4 [45]. Small differences in the thrust and efficiency were observed for the pitching foil beyond the Re of 10^4 [89]. One reason for this is that the drag coefficient varies slowly for Re
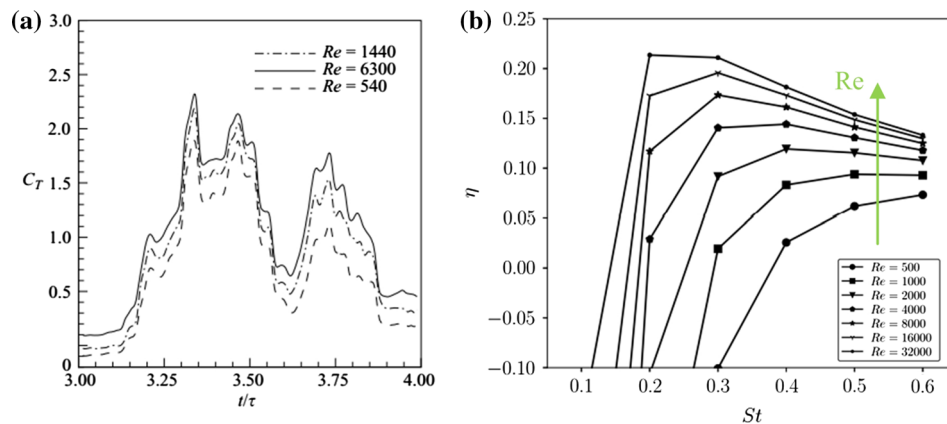
Fig. 27 Effect of Reynolds number on **a** thrust coefficient and **b** efficiency for fish pectoral fin and pitching foils. Adapted with permission from [89,100]

larger than approximately 10^4 [89]. Although there exists a significant change in force performance at different Reynolds numbers, the temporal variation of forces (Fig. 27a), i.e. the essential fluid dynamic mechanisms, is unchanged [93,100,250] within the range of Reynolds numbers studied above. This is the basis why people adopt a low-Reynolds-number condition to investigate real swimming/flying flows.

It should be pointed out that the efficiency tendency varies with Reynolds number significantly (Fig. 27b). In general, the curves of propulsive performance display the maximum value of efficiency at a particular Strouhal number (St). Swimming and flying animals are observed to cruise in a narrow range of Strouhal numbers (0.2–0.4) to maximize their efficiencies [286,287]. However, for low-Re studies [89,93], the optimal St is usually beyond the optimal range. Saadat et al. [287] implied that St is a decreasing function of speed, i.e. Re. The St number lies in a large value at low speed and levels off rapidly at high enough speed. Natural animals may also swim/fly beyond the optimal St range for some low-speed behaviours [287,288]. In fact, through the scaling argument [289], efficient cruising for animals is largely determined by the propulsor drag. When the drag coefficient shows a great variation with speed (i.e. at small Re), the value of the optimal St varies with speed. When the speed per body length is high enough (i.e. at high Re where the drag varies slightly with speed), the St seems to fall into the optimal range.

3.6 Other aspects

There are many other aspects about flying and swimming we have not addressed. They are more or less relevant to the vortex dynamics. Here, we give a brief introduction of some other aspects, e.g. stability, manoeuvrability and acoustics in swimming and flying.

3.6.1 Stability and manoeuvrability

Swimming and flying animals often exhibit remarkable manoeuvre to capture prey or avoid predator, as well as high stability in complex perturbed environments. They possess fins, wings or other specialized structures to actively or passively control the stability and manoeuvrability in swimming and flying. Swimming stability and manoeuvrability are often actively controlled by fins in fish swimming [290]. Fish and Lauder [291] summarized functions control surfaces (fins, flippers, flukes and other specialized structures) of aquatic animals. These surfaces can actively or passively generate forces and torques for stabilization or destabilizing the body to manoeuvre.

Other than fins, some fishes, e.g. boxfishes (Ostraciidae, Tetradontiformes), have a rigid body to act as a control surface [291]. Boxfishes have drawn interests of biomimetic investigations due to their remarkable rigid carapace with keel-like structures. It is considered that the specialized shape of carapace promotes stability and manoeuvrability in boxfish swimming for their capability of spinning with near-zero turning radius [292] and swimming stably under perturbations [293]. Bartol et al. [294] conducted experiments on a model of boxfish reconstructed from real specimen. By combining flow structures from PIV results and forces measurements, they found that vortices are generated by the keel structures on the carapace and produce self-correcting forces
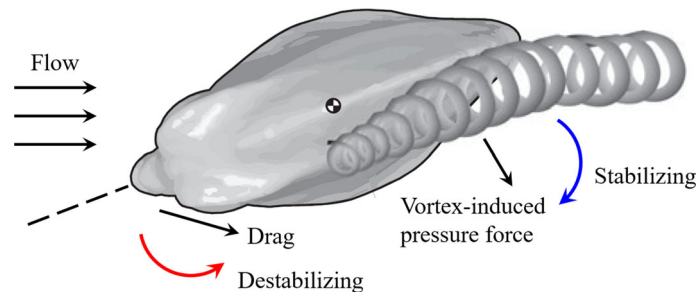
Fig. 28 Illustration of the stabilizing and destabilizing effects in boxfish swimming. Adapted with permission from [298]

to enhance swimming stability (blue arrow in Fig. 28). Bartol et al. [295,296] further examined three other species of boxfishes with distinct morphological differences and revealed that the keels in all the boxfishes are capable of producing vortices which generate self-correcting forces when the boxfishes yaw and pitch. On the other hand, observation by Blake [297] on a living boxfish showed that the boxfish exhibits remarkable manoeuvrability including turning 180°, rapidly rotating and pitching. Walker [292] also found that boxfish is capable of spinning over 150° with minimum turning radii near zero. However, for a rigid body, manoeuvrability and stability are contrary properties, and thus, a paradox arises: the morphological adaptation of boxfish is not able to enhance both stability and manoeuvrability simultaneously. To solve this paradox, van Wassenbergh et al. [298] performed experiments along with numerical simulations on boxfish models of two species with different shapes. Their results indicated that the destabilizing moments (red arrow in Fig. 28) are produced during yaw and pitch motions, while the stabilizing effects by the vortices proposed in the earlier studies [294–296] were considered to be negligible.

Insects are capable of impressive flying manoeuvres, including backward flight, climbing and descending, and also demonstrate remarkable stability during flight [138]. Thus, progresses on manoeuvrability and stability of insect flight have been made from various perspectives in the past years. Sun [138] comprehensively reviewed the researches on stability and control of insect flight. Theoretical models for flight stability analysis were summarized, and the stability properties of insect flight were concluded. There are three longitudinal natural modes: unstable slow oscillatory mode, stable fast subsidence mode and stable slow subsidence mode, and three lateral natural modes: unstable slow divergence mode, stable slow oscillatory mode and stable fast subsidence mode. The untestable modes cause the insect hovering flight dynamically unstable, which alternatively contribute to the manoeuvrability. In addition, flight stability can be enhanced by the wing deformation [131]. From experiments of humblebees with stiffened wings and normal wings, Mistick et al. [299] found that the wing flexibility increases the stability in forward flight. Zhang et al. [156] also discovered that the wing deformation improves the stability of LEV in hovering mosquito. Recently, Zhu et al. [300] studied the stability of drone fly forward flight at a wide range of speeds. They found that the drone fly is weakly unstable and approximately neutral at low and medium speeds, while the forward flight turns more unstable at high speeds because of an unstable longitudinal mode. Bode-Oke and Dong [107] numerically investigated the backward manoeuvre of butterfly using a model reconstructed from measurements and found that the upstroke, unlike forward flight, contributes more to the net force in backward flight. They also showed that the LEV occurs in the upstroke and contributes to the lift, while the LEV was previously observed during the downstroke in forward flight.

3.6.2 Acoustics

It is worth noting that animals would achieve not only high thrust/lift performance, but also good acoustics performance. For instance, the ability of owls to fly in effective silence has been scientifically confirmed by noise measurements [301], providing a distinct hunting advantage. Besides, the sound generated by flying has also important biological functions, such as sexual communication for mosquitoes [302] and aposematic signals sending for butterflies [303]. The low-noise mechanism is important in some biomimetic applications, such as ultra-quiet micro-air vehicles.

Generally, the most important noise source for swimming and flying is the surface pressure fluctuation, which is closely related to the vortex dynamics. To understand how the flow physics is related to silent flight, Jaworski and Peake [304] reviewed the previous knowledge of aerodynamic noise from owls. The foraging behaviour, morphology of owls, wing specializations (such as trailing-edge fringe, downy wing surface and
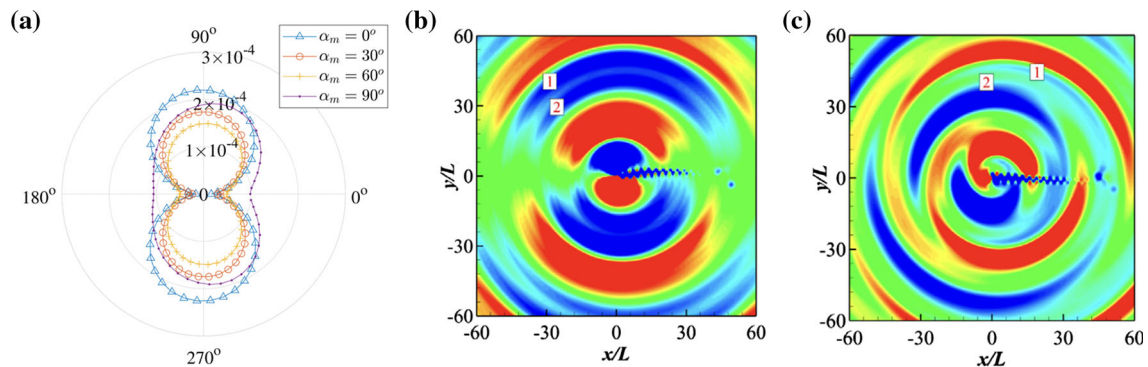
Fig. 29 a Directivity of the sound generated by rigid wings for different rotational angles (α_m) at a distance of 40 times of chord length. Instantaneous fluctuating pressure contours at the early downstroke for **b** $\alpha_m = 0°$ and **c** $\alpha_m = 90°$. Adapted with permission from [306]

leading-edge comb) were examined to determine the cause of silent flight. Ji et al. [305] found that the surface pressure fluctuation near the tip of a flapping wing can be notably reduced by a serrated trailing edge. By 2D simulation of fluid–structure–acoustics interaction, Wang and Tian [306] found that combined translational and rotational motion ($\alpha_m > 0°$) generates smaller noise than the translational one ($\alpha_m = 0°$), as shown in Fig. 29a. A dipole sound field can be transformed into a monopole one under a larger rotational angle. The delay effect is also generated by the rotational motion, thus influencing the pressure field. As shown in Fig. 29b, negative pressure pulses are formed from the upper surface at $\alpha_m = 0°$, whereas positive pulses are still generated at $\alpha_m = 90°$ (Fig. 29c). Moreover, the positive and negative pulses shift to downstream and upstream, respectively. By using 3D simulations, Wang and Tian [307] also systematically examined the effects of wing shape, prescribed motion, Reynolds number, mass ratio and flexibility on the acoustic outputs. With the positive and negative pressure pulses generated alternatively, the sound field around the flapping wing is monopole-like. Wing shape does not influence the sound directivity, but a larger wing-tip area generates larger acoustic output. An appropriate flexibility reduces the acoustic output. There are also some numerical works for the acoustic characteristics of flying animals, such as cicada [308], mosquito [309] and fruit fly [310]. For the undulatory swimmers, Wagenhoffer et al. [311] investigated their acoustic emissions using the potential flow and acoustic boundary element solver. A vertically oriented dipole dominates the transient acoustic near-field, whereas a quadrupole directivity occurs at the switch of the stoke. The acoustic pressure level of the far-field increases with frequency but decreases with the wavenumber.

4 Conclusions and perspectives

We have given an overview of the recent advances in the scope of physical models and unsteady vortex dynamics with regard to swimming and flying. The physical models include the morphological model, flexibility model, kinematics model, tethered/free model and force measurement model. As for the vortex dynamics, we focused on the physics and roles of three major vortex structures produced at the near field of swimming and flying animals, i.e. LEV, TEV and TV, as well as some factors that influence these dynamic processes, such as vortex interaction and Reynolds number effect.

Here, we further highlight the challenges and several open questions for further research: (1) although researchers have developed various models providing a mechanistic basis for understanding the physiology, movement ecology and evolution of animal swimming and flying, they are far from real animals. More accurate 3D fluid–structure interaction models, taking the distribution of bone, muscle, tissue and material property into consideration, need to be developed. (2) Investigations on the Reynolds number effect are far less than that of the upper limit of real animals. Analyses of flow field and vortex dynamics need to be extended to higher Reynolds numbers, which casts challenges to high-fidelity simulations of the flow field. (3) The physics of vortical structures, especially the TEV and TV, has attracted less attention compared with that of the LEV. The roles of the vortical structures need to be further investigated under various swimming and flying conditions. (4) Although there are some preliminary investigations [312,313] on the swimming control, where active control process was added to the present models for providing a real-time estimation of the flow state in a closed-loop control setting, how animals control the flow around them to enhance their performance needs

to be further examined. The recent interests have fostered a number of collaborations between computational fluid dynamics and artificial intelligence.

References

1. Salazar, R., Fuentes, V., Abdelkefi, A.: Classification of biological and bioinspired aquatic systems: a review. Ocean Eng. **148**, 75–114 (2018)
2. Liu, H., Ravi, S., Kolomenskiy, D., Tanaka, H.: Biomechanics and biomimetics in insect-inspired flight systems. Philos. Trans. R. Soc. B: Biol. Sci. **371**(1704), 20150390 (2016)
3. Gray, J.: Animal Locomotion. Weidenfeld & Nicolson, London (1968)
4. Videler, J.J.: Fish Swimming, vol. 10. Springer, Chapman and Hall (1993)
5. Lauder, G.V.: Fish locomotion: recent advances and new directions. Annu. Rev. Mar. Sci. **7**, 521–545 (2015)
6. Triantafyllou, M.S., Triantafyllou, G., Yue, D.: Hydrodynamics of fishlike swimming. Annu. Rev. Fluid Mech. **32**(1), 33–53 (2000)
7. Chin, D.D., Lentink, D.: Flapping wing aerodynamics: from insects to vertebrates. J. Exp. Biol. **219**(7), 920–932 (2016)
8. Wang, Z.J.: Dissecting insect flight. Annu. Rev. Fluid Mech. **37**, 183–210 (2005)
9. Liu, H., Nakata, T., Li, G., Kolomenskiy, D.: Biomechanics and biomimetics in flying and swimming. In: Industrial Biomimetics, pp. 29–80. Jenny Stanford Publishing, Boca Raton (2019)
10. Sane, S.P.: The aerodynamics of insect flight. J. Exp. Biol. **206**(23), 4191–4208 (2003)
11. Bhat, S., Zhao, J., Sheridan, J., Hourigan, K., Thompson, M.: Aspect ratio studies on insect wings. Phys. Fluids **31**(12), 121301 (2019)
12. Shyy, W., Aono, H., Chimakurthi, S.K., Trizila, P., Kang, C.-K., Cesnik, C.E., Liu, H.: Recent progress in flapping wing aerodynamics and aeroelasticity. Prog. Aerosp. Sci. **46**(7), 284–327 (2010)
13. Smits, A.J.: Undulatory and oscillatory swimming. J. Fluid Mech. **874** (2019)
14. Wu, T.Y.: Fish swimming and bird/insect flight. Annu. Rev. Fluid Mech. **43**, 25–58 (2011)
15. Triantafyllou, M.S., Weymouth, G.D., Miao, J.: Biomimetic survival hydrodynamics and flow sensing. Annu. Rev. Fluid Mech. **48**, 1–24 (2016)
16. Shelley, M.J., Zhang, J.: Flapping and bending bodies interacting with fluid flows. Annu. Rev. Fluid Mech. **43**, 449–465 (2011)
17. Fish, F., Lauder, G.V.: Passive and active flow control by swimming fishes and mammals. Annu. Rev. Fluid Mech. **38**, 193–224 (2006)
18. Fish, F.E.: The myth and reality of gray's paradox: implication of dolphin drag reduction for technology. Bioinspir. Biomimetics **1**(2), 17 (2006)
19. Costello, J.H., Colin, S.P., Dabiri, J.O., Gemmell, B.J., Lucas, K.N., Sutherland, K.R.: The hydrodynamics of jellyfish swimming. Annu. Rev. Mar. Sci. **13**, 375–396 (2021)
20. Eldredge, J.D., Jones, A.R.: Leading-edge vortices: mechanics and modeling. Annu. Rev. Fluid Mech. **51**, 75–104 (2019)
21. Izraelevitz, J.S., Kotidis, M., Triantafyllou, M.S.: Optimized kinematics enable both aerial and aquatic propulsion from a single three-dimensional flapping wing. Phys. Rev. Fluids **3**(7), 073102 (2018)
22. Webb, P.W.: The biology of fish swimming. Mechanics and physiology of animal swimming **4562** (1994)
23. Lauder, G.V., Madden, P.G.: Fish locomotion: kinematics and hydrodynamics of flexible foil-like fins. Exp. Fluids **43**(5), 641–653 (2007)
24. Triantafyllou, G.S., Triantafyllou, M.S., Grosenbaugh, M.A.: Optimal thrust development in oscillating foils with application to fish propulsion. J. Fluids Struct. **7**(2), 205–224 (1993)
25. Floryan, D., Van Buren, T., Rowley, C.W., Smits, A.J.: Scaling the propulsive performance of heaving and pitching foils. J. Fluid Mech. **822**, 386–397 (2017)
26. Chao, L.-M., Pan, G., Zhang, D., Yan, G.-X.: Numerical investigations on the force generation and wake structures of a nonsinusoidal pitching foil. J. Fluids Struct. **85**, 27–39 (2019)
27. Zhang, D., Pan, G., Chao, L., Yan, G.: Mechanisms influencing the efficiency of aquatic locomotion. Mod. Phys. Lett. B **32**(25), 1850299 (2018)
28. Zhang, D., Chao, L., Pan, G.: Ground effect on a self-propelled undulatory foil. Mod. Phys. Lett. B **32**(11), 1850135 (2018)
29. Lin, X., Wu, J., Zhang, T.: Self-directed propulsion of an unconstrained flapping swimmer at low reynolds number: hydrodynamic behaviour and scaling laws. J. Fluid Mech. **907** (2021)
30. Deng, H.-B., Xu, Y.-Q., Chen, D.-D., Dai, H., Wu, J., Tian, F.-B.: On numerical modeling of animal swimming and flight. Comput. Mech. **52**(6), 1221–1242 (2013)
31. Danos, N., Lauder, G.V.: Challenging zebrafish escape responses by increasing water viscosity. J. Exp. Biol. **215**(11), 1854–1862 (2012)
32. Breder, C.M., Jr.: The locomotion of fishes. Zoologica **4**, 159–291 (1926)
33. Videler, J., Stamhuis, E., Povel, G.: Leading-edge vortex lifts swifts. Science **306**(5703), 1960–1962 (2004)
34. Thielicke, W., Stamhuis, E.J.: The influence of wing morphology on the three-dimensional flow patterns of a flapping wing at bird scale. J. Fluid Mech. **768**, 240–260 (2015)
35. Oh, S., Lee, B., Park, H., Choi, H., Kim, S.-T.: A numerical and theoretical study of the aerodynamic performance of a hovering rhinoceros beetle (trypoxylus dichotomus). J. Fluid Mech. **885** (2020)

36. Shen, C., Sun, M.: Wing and body kinematics measurement and force analyses of landing in fruit flies. Bioinspiration & biomimetics **13**(1), 016004 (2017)
37. Bode-Oke, A.T., Zeyghami, S., Dong, H.: Aerodynamics and flow features of a damselfly in takeoff flight. Bioinspir. Biomimetics **12**(5), 056006 (2017)
38. Flammang, B.E., Lauder, G.V.: Pectoral fins aid in navigation of a complex environment by bluegill sunfish under sensory deprivation conditions. J. Exp. Biol. **216**(16), 3084–3089 (2013)
39. Wainwright, D.K., Lauder, G.V.: Tunas as a high-performance fish platform for inspiring the next generation of autonomous underwater vehicles. Bioinspir. Biomimetics **15**(3), 035007 (2020)
40. Zhang, J., Childress, S., Libchaber, A., Shelley, M.: Flexible filaments in a flowing soap film as a model for one-dimensional flags in a two-dimensional wind. Nature **408**(6814), 835–839 (2000)
41. Uddin, E., Huang, W.-X., Sung, H.J.: Interaction modes of multiple flexible flags in a uniform flow. J. Fluid Mech. **729**, 563–583 (2013)
42. Uddin, E., Huang, W.-X., Sung, H.J.: Actively flapping tandem flexible flags in a viscous flow. J. Fluid Mech. **780**, 120–142 (2015)
43. Lim, J.L., Lauder, G.V.: Mechanisms of anguilliform locomotion in fishes studied using simple three-dimensional physical models. Bioinspir. Biomimetics **11**(4), 046006 (2016)
44. Zurman-Nasution, A., Ganapathisubramani, B., Weymouth, G.: Influence of three-dimensionality on propulsive flapping. J. Fluid Mech. **886** (2020)
45. Zhang, D., Pan, G., Chao, L., Zhang, Y.: Effects of reynolds number and thickness on an undulatory self-propelled foil. Phys. Fluids **30**(7), 071902 (2018)
46. Zhang, C., Huang, H., Lu, X.-Y.: Effect of trailing-edge shape on the self-propulsive performance of heaving flexible plates. J. Fluid Mech. **887** (2020)
47. Koehler, C., Liang, Z., Gaston, Z., Wan, H., Dong, H.: 3d reconstruction and analysis of wing deformation in free-flying dragonflies. J. Exp. Biol. **215**(17), 3018–3027 (2012)
48. Kern, S., Koumoutsakos, P.: Simulations of optimized anguilliform swimming. J. Exp. Biol. **209**(24), 4841–4857 (2006)
49. Zhu, Q., Wolfgang, M., Yue, D., Triantafyllou, M.: Three-dimensional flow structures and vorticity control in fish-like swimming. J. Fluid Mech. **468**, 1–28 (2002)
50. Tanaka, H., Li, G., Uchida, Y., Nakamura, M., Ikeda, T., Liu, H.: Measurement of time-varying kinematics of a dolphin in burst accelerating swimming. PLoS ONE **14**(1), 0210860 (2019)
51. Huang, Q., Zhang, D., Pan, G.: Computational model construction and analysis of the hydrodynamics of a rhinoptera javanica. IEEE Access **8**, 30410–30420 (2020)
52. Zou, P.-Y., Lai, Y.-H., Yang, J.-T.: Effects of phase lag on the hovering flight of damselfly and dragonfly. Phys. Rev. E **100**(6), 063102 (2019)
53. Xu, R., Zhang, X., Liu, H.: Effects of wing-to-body mass ratio on insect flapping flights. Phys. Fluids **33**(2), 021902 (2021)
54. Nakata, T., Liu, H.: Aerodynamic performance of a hovering hawkmoth with flexible wings: a computational approach. Proc. R. Soc. B: Biol. Sci. **279**(1729), 722–731 (2012)
55. Aono, H., Liang, F., Liu, H.: Near-and far-field aerodynamics in insect hovering flight: an integrated computational study. J. Exp. Biol. **211**(2), 239–257 (2008)
56. Liu, L.-G., Du, G., Sun, M.: Aerodynamic-force production mechanisms in hovering mosquitoes. J. Fluid Mech. **898** (2020)
57. Watts, P., Mitchell, E.J., Swartz, S.M.: A computational model for estimating the mechanics of horizontal flapping flight in bats: model description and validation. J. Exp. Biol. **204**(16), 2873–2898 (2001)
58. Wang, S., Zhang, X., He, G., Liu, T.: Numerical simulation of unsteady flows over a slow-flying bat. Theor. Appl. Mech. Lett. **5**(1), 5–8 (2015)
59. Wang, S., Zhang, X., He, G., Liu, T.: Lift enhancement by bats' dynamically changing wingspan. J. R. Soc. Interface **12**(113), 20150821 (2015)
60. Maeda, M., Nakata, T., Kitamura, I., Tanaka, H., Liu, H.: Quantifying the dynamic wing morphing of hovering hummingbird. R. Soc. Open Sci. **4**(9), 170307 (2017)
61. Luo, H., Dai, H., Das, S.S., Song, J., Doyle, J.: Toward high-fidelity modeling of the fluid-structure interaction for insect wings. In: 50th AIAA Aerospace Sciences Meeting Including the New Horizons Forum and Aerospace Exposition, p. 1212 (2012)
62. Chang, E., Matloff, L.Y., Stowers, A.K., Lentink, D.: Soft biohybrid morphing wings with feathers underactuated by wrist and finger motion. Sci. Robotics **5**(38) (2020)
63. Huang, W.-X., Sung, H.J.: Three-dimensional simulation of a flapping flag in a uniform flow. J. Fluid Mech. **653**, 301–336 (2010)
64. Huang, W.-X., Shin, S.J., Sung, H.J.: Simulation of flexible filaments in a uniform flow by the immersed boundary method. J. Comput. Phys. **226**(2), 2206–2228 (2007)
65. Huang, W.-X., Sung, H.J.: An immersed boundary method for fluid-flexible structure interaction. Comput. Methods Appl. Mech. Eng. **198**(33–36), 2650–2661 (2009)
66. Shahzad, A., Tian, F.-B., Young, J., Lai, J.C.: Effects of flexibility on the hovering performance of flapping wings with different shapes and aspect ratios. J. Fluids Struct. **81**, 69–96 (2018)
67. Tian, F.-B., Luo, H., Song, J., Lu, X.-Y.: Force production and asymmetric deformation of a flexible flapping wing in forward flight. J. Fluids Struct. **36**, 149–161 (2013)
68. Wang, C., Ren, F., Tang, H.: Enhancing propulsion performance of a flexible heaving foil through dynamically adjusting its flexibility. Bioinspir. Biomimetics **14**(6), 064002 (2019)
69. Ryu, J., Park, S.G., Huang, W.-X., Sung, H.J.: Hydrodynamics of a three-dimensional self-propelled flexible plate. Phys. Fluids **31**(2), 021902 (2019)
70. Wang, S., Ryu, J., He, G.-Q., Qin, F., Sung, H.J.: A self-propelled flexible plate with a navier slip surface. Phys. Fluids **32**(2), 021906 (2020)

71. Tian, F.-B.: A numerical study of linear and nonlinear kinematic models in fish swimming with the dsd/sst method. Comput. Mech. **55**(3), 469–477 (2015)
72. Chen, Y., Gravish, N., Desbiens, A.L., Malka, R., Wood, R.J.: Experimental and computational studies of the aerodynamic performance of a flapping and passively rotating insect wing. J. Fluid Mech. **791**, 1–33 (2016)
73. Lei, M., Li, C.: The aerodynamic performance of passive wing pitch in hovering flight. Phys. Fluids **32**(5), 051902 (2020)
74. Ishihara, D., Horie, T.: Passive mechanism of pitch recoil in flapping insect wings. Bioinspir. Biomimetics **12**(1), 016008 (2016)
75. Zeyghami, S., Zhong, Q., Liu, G., Dong, H.: Passive pitching of a flapping wing in turning flight. AIAA J. **57**(9), 3744–3752 (2019)
76. Zhao, F., Qadri, M.M., Wang, Z., Tang, H.: Flow-energy harvesting using a fully passive flapping foil: a guideline on design and operation. Int. J. Mech. Sci. **197**, 106323 (2021)
77. Qadri, M.M., Zhao, F., Tang, H.: Fluid-structure interaction of a fully passive flapping foil for flow energy extraction. Int. J. Mech. Sci. **177**, 105587 (2020)
78. Qadri, M.M., Shahzad, A., Zhao, F., Tang, H., et al.: An experimental investigation of a passively flapping foil in energy harvesting mode (2019)
79. Tytell, E.D., Hsu, C.-Y., Williams, T.L., Cohen, A.H., Fauci, L.J.: Interactions between internal forces, body stiffness, and fluid environment in a neuromechanical model of lamprey swimming. Proc. Natl. Acad. Sci. **107**(46), 19832–19837 (2010)
80. Combes, S., Daniel, T.: Flexural stiffness in insect wings ii. spatial distribution and dynamic wing bending. J. Exp. Biol. **206**(17), 2989–2997 (2003)
81. Shahzad, A., Tian, F.-B., Young, J., Lai, J.C.: Effects of hawkmoth-like flexibility on the aerodynamic performance of flapping wings with different shapes and aspect ratios. Phys. Fluids **30**(9), 091902 (2018)
82. Webb, P.W.: Form and function in fish swimming. Sci. Am. **251**(1), 72–83 (1984)
83. Khalid, M.S.U., Wang, J., Dong, H., Liu, M.: Flow transitions and mapping for undulating swimmers. Phys. Rev. Fluids **5**(6), 063104 (2020)
84. Tytell, E.D., Lauder, G.V.: The hydrodynamics of eel swimming: I. Wake structure. J. Exp. Biol. **207**(11), 1825–1841 (2004)
85. Borazjani, I., Sotiropoulos, F.: On the role of form and kinematics on the hydrodynamics of self-propelled body/caudal fin swimming. J. Exp. Biol. **213**(1), 89–107 (2010)
86. Borazjani, I., Sotiropoulos, F.: Numerical investigation of the hydrodynamics of carangiform swimming in the transitional and inertial flow regimes. J. Exp. Biol. **211**(10), 1541–1558 (2008)
87. Zhang, J.-D., Sung, H.J., Huang, W.-X.: Specialization of tuna: a numerical study on the function of caudal keels. Phys. Fluids **32**(11), 111902 (2020)
88. Senturk, U., Smits, A.J.: Numerical simulations of the flow around a square pitching panel. J. Fluids Struct. **76**, 454–468 (2018)
89. Senturk, U., Smits, A.J.: Reynolds number scaling of the propulsive performance of a pitching airfoil. AIAA J. **57**(7), 2663–2669 (2019)
90. Van Buren, T., Floryan, D., Smits, A.J.: Scaling and performance of simultaneously heaving and pitching foils. AIAA J. **57**(9), 3666–3677 (2019)
91. Floryan, D., Van Buren, T., Smits, A.J.: Large-amplitude oscillations of foils for efficient propulsion. Phys. Rev. Fluids **4**(9), 093102 (2019)
92. Schouveiler, L., Hover, F., Triantafyllou, M.: Performance of flapping foil propulsion. J. Fluids Struct. **20**(7), 949–959 (2005)
93. Dong, H., Mittal, R., Najjar, F.: Wake topology and hydrodynamic performance of low-aspect-ratio flapping foils. J. Fluid Mech. **566**, 309–343 (2006)
94. Zhang, D., Huang, Q.-G., Pan, G., Yang, L.-M., Huang, W.-X.: Vortex dynamics and hydrodynamic performance enhancement mechanism in batoid fish oscillatory swimming. J. Fluid Mech. **930** (2022)
95. Thekkethil, N., Sharma, A., Agrawal, A.: Three-dimensional biological hydrodynamics study on various types of batoid fishlike locomotion. Phys. Rev. Fluids **5**(2), 023101 (2020)
96. Bottom Ii, R., Borazjani, I., Blevins, E., Lauder, G.: Hydrodynamics of swimming in stingrays: numerical simulations and the role of the leading-edge vortex. J. Fluid Mech. **788**, 407–443 (2016)
97. Blevins, E.L., Lauder, G.V.: Rajiform locomotion: three-dimensional kinematics of the pectoral fin surface during swimming in the freshwater stingray potamotrygon orbignyi. J. Exp. Biol. **215**(18), 3231–3241 (2012)
98. Su, G., Shen, H., Li, N., Zhu, Y., Su, Y.: Numerical investigation of the hydrodynamics of stingray swimming under self-propulsion. J. Fluids Struct. **106**, 103383 (2021)
99. Standen, E., Lauder, G.V.: Dorsal and anal fin function in bluegill sunfish lepomis macrochirus: three-dimensional kinematics during propulsion and maneuvering. J. Exp. Biol. **208**(14), 2753–2763 (2005)
100. Bozkurttas, M., Mittal, R., Dong, H., Lauder, G., Madden, P.: Low-dimensional models and performance scaling of a highly deformable fish pectoral fin. J. Fluid Mech. **631**, 311–342 (2009)
101. Wang, J., Ren, Y., Li, C., Dong, H.: Computational investigation of wing-body interaction and its lift enhancement effect in hummingbird forward flight. Bioinspir. biomimetics **14**(4), 046010 (2019)
102. Liu, Y., Sun, M.: Wing kinematics measurement and aerodynamics of hovering dronefies. J. Exp. Biol. **211**(13), 2014–2025 (2008)
103. Wan, H., Dong, H., Gai, K.: Computational investigation of cicada aerodynamics in forward flight. J. R. Soc. Interface **12**(102), 20141116 (2015)
104. Song, J., Tobalske, B.W., Powers, D.R., Hedrick, T.L., Luo, H.: Three-dimensional simulation for fast forward flight of a calliope hummingbird. R. Soc. Open Sci. **3**(6), 160230 (2016)
105. Li, C., Dong, H.: Wing kinematics measurement and aerodynamics of a dragonfly in turning flight. Bioinspir. Biomimetics **12**(2), 026001 (2017)
106. Bode-Oke, A.T., Zeyghami, S., Dong, H.: Flying in reverse: kinematics and aerodynamics of a dragonfly in backward free flight. J. R. Soc. Interface **15**(143), 20180102 (2018)

107. Bode-Oke, A.T., Dong, H.: The reverse flight of a monarch butterfly (danaus plexippus) is characterized by a weight-supporting upstroke and postural changes. J. R. Soc. Interface **17**(167), 20200268 (2020)
108. Ellington, C.P., Van Den Berg, C., Willmott, A.P., Thomas, A.L.: Leading-edge vortices in insect flight. Nature **384**(6610), 626–630 (1996)
109. Fuchiwaki, M., Kuroki, T., Tanaka, K., Tababa, T.: Dynamic behavior of the vortex ring formed on a butterfly wing. Exp. Fluids **54**(1), 1–12 (2013)
110. Henningsson, P., Michaelis, D., Nakata, T., Schanz, D., Geisler, R., Schröder, A., Bomphrey, R.J.: The complex aerodynamic footprint of desert locusts revealed by large-volume tomographic particle image velocimetry. J. R. Soc. Interface **12**(108), 20150119 (2015)
111. Thomas, A.L., Taylor, G.K., Srygley, R.B., Nudds, R.L., Bomphrey, R.J.: Dragonfly flight: free-flight and tethered flow visualizations reveal a diverse array of unsteady lift-generating mechanisms, controlled primarily via angle of attack. J. Exp. Biol. **207**(24), 4299–4323 (2004)
112. Bomphrey, R.J., Taylor, G.K., Thomas, A.L.: Smoke visualization of free-flying bumblebees indicates independent leading-edge vortices on each wing pair. In: Animal Locomotion, pp. 249–259. Springer, Berlin (2010)
113. Hubel, T.Y., Riskin, D.K., Swartz, S.M., Breuer, K.S.: Wake structure and wing kinematics: the flight of the lesser dog-faced fruit bat, cynopterus brachyotis. J. Exp. Biol. **213**(20), 3427–3440 (2010)
114. Pournazeri, S., Segre, P.S., Princevac, M., Altshuler, D.L.: Hummingbirds generate bilateral vortex loops during hovering: evidence from flow visualization. Exp. Fluids **54**(1), 1–11 (2013)
115. Flammang, B.E., Lauder, G.V., Troolin, D.R., Strand, T.: Volumetric imaging of shark tail hydrodynamics reveals a three-dimensional dual-ring vortex wake structure. Proc. R. Soc. B: Biol. Sci. **278**(1725), 3670–3678 (2011)
116. Flammang, B.E., Lauder, G.V., Troolin, D.R., Strand, T.E.: Volumetric imaging of fish locomotion. Biol. Let. **7**(5), 695–698 (2011)
117. Tytell, E.D., Lauder, G.V.: Hydrodynamics of the escape response in bluegill sunfish, lepomis macrochirus. J. Exp. Biol. **211**(21), 3359–3369 (2008)
118. Van Buren, T., Floryan, D., Wei, N., Smits, A.J.: Flow speed has little impact on propulsive characteristics of oscillating foils. Phys. Rev. Fluids **3**(1), 013103 (2018)
119. Lighthill, M.: Note on the swimming of slender fish. J. Fluid Mech. **9**(2), 305–317 (1960)
120. Liu, G., Ren, Y., Dong, H., Akanyeti, O., Liao, J.C., Lauder, G.V.: Computational analysis of vortex dynamics and performance enhancement due to body-fin and fin-fin interactions in fish-like locomotion. J. Fluid Mech. **829**, 65–88 (2017)
121. Han, P., Lauder, G.V., Dong, H.: Hydrodynamics of median-fin interactions in fish-like locomotion: Effects of fin shape and movement. Phys. Fluids **32**(1), 011902 (2020)
122. Borazjani, I., Sotiropoulos, F.: Numerical investigation of the hydrodynamics of anguilliform swimming in the transitional and inertial flow regimes. J. Exp. Biol. **212**(4), 576–592 (2009)
123. Fish, F.E., Schreiber, C.M., Moored, K.W., Liu, G., Dong, H., Bart-Smith, H.: Hydrodynamic performance of aquatic flapping: efficiency of underwater flight in the manta. Aerospace **3**(3), 20 (2016)
124. Xiao, Q., Hu, J., Liu, H.: Effect of torsional stiffness and inertia on the dynamics of low aspect ratio flapping wings. Bioinspir. Biomimetics **9**(1), 016008 (2014)
125. Bale, R., Hao, M., Bhalla, A.P.S., Patel, N., Patankar, N.A.: Gray's paradox: a fluid mechanical perspective. Sci. Rep. **4**(1), 1–5 (2014)
126. Lighthill, M.J.: Large-amplitude elongated-body theory of fish locomotion. Proc. R. Soc. Lond. Ser. B. Biol. Sci. **179**(1055), 125–138 (1971)
127. Cheng, J.-Y., Blickhan, R.: Note on the calculation of propeller efficiency using elongated body theory. J. Exp. Biol. **192**(1), 169–177 (1994)
128. Maertens, A., Triantafyllou, M.S., Yue, D.K.: Efficiency of fish propulsion. Bioinspir. Biomimetics **10**(4), 046013 (2015)
129. Fish, F.E., Rohr, J.: Review of dolphin hydrodynamics and swimming performance (1999)
130. Bale, R., Hao, M., Bhalla, A.P.S., Patankar, N.A.: Energy efficiency and allometry of movement of swimming and flying animals. Proc. Natl. Acad. Sci. **111**(21), 7517–7521 (2014)
131. Liu, H., Kolomenskiy, D., Nakata, T., Li, G.: Unsteady bio-fluid dynamics in flying and swimming. Acta. Mech. Sin. **33**(4), 663–684 (2017)
132. Muijres, F.T., Johansson, L.C., Hedenström, A.: Leading edge vortex in a slow-flying passerine. Biol. Let. **8**(4), 554–557 (2012)
133. Muijres, F., Johansson, L.C., Barfield, R., Wolf, M., Spedding, G., Hedenström, A.: Leading-edge vortex improves lift in slow-flying bats. Science **319**(5867), 1250–1253 (2008)
134. Windes, P., Fan, X., Bender, M., Tafti, D.K., Müller, R.: A computational investigation of lift generation and power expenditure of pratt's roundleaf bat (hipposideros pratti) in forward flight. PLoS ONE **13**(11), 0207613 (2018)
135. Windes, P., Tafti, D.K., Müller, R.: Determination of spatial fidelity required to accurately mimic the flight dynamics of a bat. Bioinspir. Biomimetics **14**(6), 066011 (2019)
136. Lentink, D., Dickinson, M.H.: Rotational accelerations stabilize leading edge vortices on revolving fly wings. J. Exp. Biol. **212**(16), 2705–2719 (2009)
137. Johansson, L.C., Norberg, R.Å.: Delta-wing function of webbed feet gives hydrodynamic lift for swimming propulsion in birds. Nature **424**(6944), 65–68 (2003)
138. Sun, M.: Insect flight dynamics: stability and control. Rev. Mod. Phys. **86**(2), 615 (2014)
139. Wu, J.C.: Theory for aerodynamic force and moment in viscous flows. AIAA J. **19**(4), 432–441 (1981)
140. Wu, J.-Z., Ma, H.-Y., Zhou, M.-D.: Vorticity and Vortex Dynamics. Springer, Berlin (2007)
141. Wu, J.-Z., Lu, X.-Y., Zhuang, L.-X.: Integral force acting on a body due to local flow structures. J. Fluid Mech. **576**, 265–286 (2007)
142. Kang, L., Liu, L., Su, W., Wu, J.: Minimum-domain impulse theory for unsteady aerodynamic force. Phys. Fluids **30**(1), 016107 (2018)

143. Werner, N.H., Chung, H., Wang, J., Liu, G., Cimbala, J.M., Dong, H., Cheng, B.: Radial planetary vorticity tilting in the leading-edge vortex of revolving wings. Phys. Fluids **31**(4), 041902 (2019)
144. Maxworthy, T.: The formation and maintenance of a leading-edge vortex during the forward motion of an animal wing. J. Fluid Mech. **587**, 471–475 (2007)
145. Cheng, B., Sane, S.P., Barbera, G., Troolin, D.R., Strand, T., Deng, X.: Three-dimensional flow visualization and vorticity dynamics in revolving wings. Exp. Fluids **54**(1), 1423 (2013)
146. Wojcik, C.J., Buchholz, J.H.: Vorticity transport in the leading-edge vortex on a rotating blade. J. Fluid Mech. **743**, 249–261 (2014)
147. Garmann, D., Visbal, M.: Dynamics of revolving wings for various aspect ratios. J. Fluid Mech. **748**, 932–956 (2014)
148. Jardin, T., David, L.: Coriolis effects enhance lift on revolving wings. Phys. Rev. E **91**(3), 031001 (2015)
149. Phillips, N., Knowles, K., Bomphrey, R.J.: The effect of aspect ratio on the leading-edge vortex over an insect-like flapping wing. Bioinspir. Biomimetics **10**(5), 056020 (2015)
150. Phillips, N., Knowles, K., Bomphrey, R.J.: Petiolate wings: effects on the leading-edge vortex in flapping flight. Interface Focus **7**(1), 20160084 (2017)
151. Du, G., Sun, M.: Effects of wing deformation on aerodynamic forces in hovering hoverflies. J. Exp. Biol. **213**(13), 2273–2283 (2010)
152. Engels, T., Kolomenskiy, D., Schneider, K., Farge, M., Lehmann, F.-O., Sesterhenn, J.: Helical vortices generated by flapping wings of bumblebees. Fluid Dyn. Res. **50**(1), 011419 (2018)
153. Srygley, R., Thomas, A.: Unconventional lift-generating mechanisms in free-flying butterflies. Nature **420**(6916), 660–664 (2002)
154. Lin, Y.-J., Chang, S.-K., Lai, Y.-H., Yang, J.-T.: Beneficial wake-capture effect for forward propulsion with a restrained wing-pitch motion of a butterfly. R. Soc. Open Sci. **8**(8), 202172 (2021)
155. Liu, Y., Lozano, A.D., Hedrick, T.L., Li, C.: Comparison of experimental and numerical studies on the flow structures of hovering hawkmoths. J. Fluids Struct. **107**, 103405 (2021)
156. Zhang, J.-D., Huang, W.-X.: On the role of vortical structures in aerodynamic performance of a hovering mosquito. Phys. Fluids **31**(5), 051906 (2019)
157. Linehan, T., Mohseni, K.: On the maintenance of an attached leading-edge vortex via model bird alula. J. Fluid Mech. **897** (2020)
158. Lentink, D., Dickson, W.B., Van Leeuwen, J.L., Dickinson, M.H.: Leading-edge vortices elevate lift of autorotating plant seeds. Science **324**(5933), 1438–1440 (2009)
159. Seale, M., Nakayama, N.: From passive to informed: mechanical mechanisms of seed dispersal. New Phytol. **225**(2), 653–658 (2020)
160. NORBERG, R.Å.: Autorotation, self-stability, and structure of single-winged fruits and seeds (samaras) with comparative remarks on animal flight. Biol. Rev. **48**(4), 561–596 (1973)
161. Salcedo, E., Treviño, C., Vargas, R.O., Martínez-Suástegui, L.: Stereoscopic particle image velocimetry measurements of the three-dimensional flow field of a descending autorotating mahogany seed (swietenia macrophylla). J. Exp. Biol. **216**(11), 2017–2030 (2013)
162. Lee, I., Choi, H.: Flight of a falling maple seed. Phys. Rev. Fluids **2**(9), 090511 (2017)
163. Lee, I., Choi, H.: Scaling law for the lift force of autorotating falling seeds at terminal velocity. J. Fluid Mech. **835**, 406–420 (2018)
164. Borazjani, I., Daghooghi, M.: The fish tail motion forms an attached leading edge vortex. Proc. R. Soc. B: Biol. Sci. **280**(1756), 20122071 (2013)
165. Zhu, J., White, C., Wainwright, D.K., Di Santo, V., Lauder, G.V., Bart-Smith, H.: Tuna robotics: A high-frequency experimental platform exploring the performance space of swimming fishes. Sci. Robotics **4**(34) (2019)
166. Jones, A., Ford, C.P., Babinsky, H.: Three-dimensional effects on sliding and waving wings. J. Aircr. **48**(2), 633–644 (2011)
167. Dickinson, M.H., Lehmann, F.-O., Sane, S.P.: Wing rotation and the aerodynamic basis of insect flight. Science **284**(5422), 1954–1960 (1999)
168. Jones, A., Babinsky, H.: Unsteady lift generation on rotating wings at low Reynolds numbers. J. Aircr. **47**(3), 1013–1021 (2010)
169. Ohmi, K., Coutanceau, M., Loc, T.P., Dulieu, A.: Vortex formation around an oscillating and translating airfoil at large incidences. J. Fluid Mech. **211**, 37–60 (1990)
170. Panda, J., Zaman, K.B.: Experimental investigation of the flow field of an oscillating airfoil and estimation of lift from wake surveys. J. Fluid Mech. **265**, 65–95 (1994)
171. Bomphrey, R.J., Nakata, T., Phillips, N., Walker, S.M.: Smart wing rotation and trailing-edge vortices enable high frequency mosquito flight. Nature **544**(7648), 92–95 (2017)
172. Zhu, H.J., Sun, M.: Unsteady aerodynamic force mechanisms of a hoverfly hovering with a short stroke-amplitude. Phys. Fluids **29**(8), 081901 (2017)
173. Shekarriz, A., Fu, T., Katz, J., Huang, T.: Near-field behavior of a tip vortex. AIAA J. **31**(1), 112–118 (1993)
174. Spalart, P.R.: Airplane trailing vortices. Annu. Rev. Fluid Mech. **30**(1), 107–138 (1998)
175. Gerz, T., Holzäpfel, F., Darracq, D.: Commercial aircraft wake vortices. Prog. Aerosp. Sci. **38**(3), 181–208 (2002)
176. Leete, K.M., Gee, K.L., Liu, J., Wall, A.T.: Coherence analysis of the noise from a simulated highly heated laboratory-scale jet. AIAA J. **58**(8), 3426–3435 (2020)
177. Gerz, T., Holzapfel, F.: Wing-tip vortices, turbulence, and the distribution of emissions. AIAA J. **37**(10), 1270–1276 (1999)
178. Birch, D., Lee, T., Mokhtarian, F., Kafyeke, F.: Structure and induced drag of a tip vortex. J. Aircr. **41**(5), 1138–1145 (2004)
179. Ringuette, M.J., Milano, M., Gharib, M.: Role of the tip vortex in the force generation of low-aspect-ratio normal flat plates. J. Fluid Mech. **581**, 453–468 (2007)
180. Kim, D., Gharib, M.: Experimental study of three-dimensional vortex structures in translating and rotating plates. Exp. Fluids **49**(1), 329–339 (2010)

181. Carr, Z., Chen, C., Ringuette, M.: Finite-span rotating wings: three-dimensional vortex formation and variations with aspect ratio. Exp. Fluids **54**(2), 1–26 (2013)
182. Carr, Z.R., DeVoria, A.C., Ringuette, M.J.: Aspect-ratio effects on rotating wings: circulation and forces. J. Fluid Mech. **767**, 497–525 (2015)
183. Birch, D., Lee, T.: Investigation of the near-field tip vortex behind an oscillating wing. J. Fluid Mech. **544**, 201–241 (2005)
184. Li, C., Dong, H., Cheng, B.: Tip vortices formation and evolution of rotating wings at low Reynolds numbers. Phys. Fluids **32**(2), 021905 (2020)
185. Poelma, C., Dickson, W., Dickinson, M.: Time-resolved reconstruction of the full velocity field around a dynamically-scaled flapping wing. Exp. Fluids **41**(2), 213–225 (2006)
186. Hartloper, C., Kinzel, M., Rival, D.E.: On the competition between leading-edge and tip-vortex growth for a pitching plate. Exp. Fluids **54**(1), 1–11 (2013)
187. Yilmaz, T.O., Rockwell, D.: Flow structure on finite-span wings due to pitch-up motion. J. Fluid Mech. **691**, 518–545 (2012)
188. Dong, H., Bozkurttas, M., Mittal, R., Madden, P., Lauder, G.: Computational modelling and analysis of the hydrodynamics of a highly deformable fish pectoral fin. J. Fluid Mech. **645**, 345–373 (2010)
189. Liu, G., Dong, H., Li, C.: Vortex dynamics and new lift enhancement mechanism of wing-body interaction in insect forward flight. J. Fluid Mech. **795**, 634–651 (2016)
190. Shyy, W., Trizila, P., Kang, C.-K., Aono, H.: Can tip vortices enhance lift of a flapping wing? AIAA J. **47**(2), 289–293 (2009)
191. Newbolt, J.W., Zhang, J., Ristroph, L.: Flow interactions between uncoordinated flapping swimmers give rise to group cohesion. Proc. Natl. Acad. Sci. **116**(7), 2419–2424 (2019)
192. Lissaman, P., Shollenberger, C.A.: Formation flight of birds. Science **168**(3934), 1003–1005 (1970)
193. Weihs, D.: Hydromechanics of fish schooling. Nature **241**(5387), 290–291 (1973)
194. Nakata, T., Henningsson, P., Lin, H.-T., Bomphrey, R.J.: Recent progress on the flight of dragonflies and damselflies. Int. J. Odonatol. **23**(1), 41–49 (2020)
195. Peng, L., Zheng, M., Pan, T., Su, G., Li, Q.: Tandem-wing interactions on aerodynamic performance inspired by dragonfly hovering. R. Soc. Open Sci. **8**(8), 202275 (2021)
196. Matthews, D., Lauder, G.V.: Fin-fin interactions during locomotion in a simplified biomimetic fish model. Bioinspir. Biomimetics (2021)
197. Zhu, X., He, G., Zhang, X.: Flow-mediated interactions between two self-propelled flapping filaments in tandem configuration. Phys. Rev. Lett. **113**(23), 238105 (2014)
198. Portugal, S.J., Hubel, T.Y., Fritz, J., Heese, S., Trobe, D., Voelkl, B., Hailes, S., Wilson, A.M., Usherwood, J.R.: Upwash exploitation and downwash avoidance by flap phasing in ibis formation flight. Nature **505**(7483), 399–402 (2014)
199. Alaminos-Quesada, J., Fernandez-Feria, R.: Aerodynamics of heaving and pitching foils in tandem from linear potential theory. AIAA J. **58**(1), 37–52 (2020)
200. Alaminos-Quesada, J., Fernandez-Feria, R.: Propulsion performance of tandem flapping foils with chordwise prescribed deflection from linear potential theory. Phys. Rev. Fluids **6**(1), 013102 (2021)
201. Becker, A.D., Masoud, H., Newbolt, J.W., Shelley, M., Ristroph, L.: Hydrodynamic schooling of flapping swimmers. Nat. Commun. **6**(1), 1–8 (2015)
202. Ramananarivo, S., Fang, F., Oza, A., Zhang, J., Ristroph, L.: Flow interactions lead to orderly formations of flapping wings in forward flight. Phys. Rev. Fluids **1**(7), 071201 (2016)
203. Lagopoulos, N., Weymouth, G., Ganapathisubramani, B.: Deflected wake interaction of tandem flapping foils. J. Fluid Mech. **903** (2020)
204. Akhtar, I., Mittal, R., Lauder, G.V., Drucker, E.: Hydrodynamics of a biologically inspired tandem flapping foil configuration. Theor. Comput. Fluid Dyn. **21**(3), 155–170 (2007)
205. Zheng, Y., Wu, Y., Tang, H.: An experimental study on the forewing-hindwing interactions in hovering and forward flights. Int. J. Heat Fluid Flow **59**, 62–73 (2016)
206. Jia, L.-B., Yin, X.-Z.: Passive oscillations of two tandem flexible filaments in a flowing soap film. Phys. Rev. Lett. **100**(22), 228104 (2008)
207. Jia, L.-B., Yin, X.-Z.: Response modes of a flexible filament in the wake of a cylinder in a flowing soap film. Phys. Fluids **21**(10), 101704 (2009)
208. Mazharmanesh, S., Young, J., Tian, F.-B., Lai, J.C.: Energy harvesting of two inverted piezoelectric flags in tandem, side-by-side and staggered arrangements. Int. J. Heat Fluid Flow **83**, 108589 (2020)
209. Streitlien, K., Triantafyllou, G.S., Triantafyllou, M.S.: Efficient foil propulsion through vortex control. AIAA J. **34**(11), 2315–2319 (1996)
210. Alben, S.: On the swimming of a flexible body in a vortex street. J. Fluid Mech. **635**, 27–45 (2009)
211. Wang, W., Huang, H., Lu, X.-Y.: Self-propelled plate in wakes behind tandem cylinders. Phys. Rev. E **100**(3), 033114 (2019)
212. Maybury, W.J., Lehmann, F.-O.: The fluid dynamics of flight control by kinematic phase lag variation between two robotic insect wings. J. Exp. Biol. **207**(26), 4707–4726 (2004)
213. Wang, Z.J., Russell, D.: Effect of forewing and hindwing interactions on aerodynamic forces and power in hovering dragonfly flight. Phys. Rev. Lett. **99**(14), 148101 (2007)
214. Xie, C.-M., Huang, W.-X.: Vortex interactions between forewing and hindwing of dragonfly in hovering flight. Theor. Appl. Mech. Lett. **5**(1), 24–29 (2015)
215. Ristroph, L., Zhang, J.: Anomalous hydrodynamic drafting of interacting flapping flags. Phys. Rev. Lett. **101**(19), 194502 (2008)
216. Alben, S.: Wake-mediated synchronization and drafting in coupled flags. J. Fluid Mech. **641**, 489–496 (2009)
217. Kim, S., Huang, W.-X., Sung, H.J.: Constructive and destructive interaction modes between two tandem flexible flags in viscous flow. J. Fluid Mech. **661**, 511–521 (2010)

218. Boschitsch, B.M., Dewey, P.A., Smits, A.J.: Propulsive performance of unsteady tandem hydrofoils in an in-line configuration. Phys. Fluids **26**(5), 051901 (2014)
219. Kurt, M., Moored, K.W.: Flow interactions of two-and three-dimensional networked bio-inspired control elements in an in-line arrangement. Bioinspir. Biomimetics **13**(4), 045002 (2018)
220. Han, P., Pan, Y., Liu, G., Dong, H.: Propulsive performance and vortex wakes of multiple tandem foils pitching in-line. J. Fluids Struct. **108**, 103422 (2022)
221. Peng, Z.-R., Huang, H., Lu, X.-Y.: Hydrodynamic schooling of multiple self-propelled flapping plates. J. Fluid Mech. **853**, 587–600 (2018)
222. Lin, X., Wu, J., Zhang, T., Yang, L.: Self-organization of multiple self-propelling flapping foils: energy saving and increased speed. J. Fluid Mech. **884** (2020)
223. Zhang, J.-D., Huang, W.-X.: Numerical model and hydrodynamic performance of tuna finlets. Theor. Appl. Mech. Lett. 100322 (2022)
224. Liao, J.C., Beal, D.N., Lauder, G.V., Triantafyllou, M.S.: The kármán gait: novel body kinematics of rainbow trout swimming in a vortex street. J. Exp. Biol. **206**(6), 1059–1073 (2003)
225. Taguchi, M., Liao, J.C.: Rainbow trout consume less oxygen in turbulence: the energetics of swimming behaviors at different speeds. J. Exp. Biol. **214**(9), 1428–1436 (2011)
226. Drucker, E.G., Lauder, G.V.: Locomotor function of the dorsal fin in teleost fishes: experimental analysis of wake forces in sunfish. J. Exp. Biol. **204**(17), 2943–2958 (2001)
227. Drucker, E.G., Lauder, G.V.: Locomotor function of the dorsal fin in rainbow trout: kinematic patterns and hydrodynamic forces. J. Exp. Biol. **208**(23), 4479–4494 (2005)
228. Standen, E., Lauder, G.V.: Hydrodynamic function of dorsal and anal fins in brook trout (salvelinus fontinalis). J. Exp. Biol. **210**(2), 325–339 (2007)
229. Wang, J., Wainwright, D.K., Lindengren, R.E., Lauder, G.V., Dong, H.: Tuna locomotion: a computational hydrodynamic analysis of finlet function. J. R. Soc. Interface **17**(165), 20190590 (2020)
230. Gazzola, M., Argentina, M., Mahadevan, L.: Scaling macroscopic aquatic locomotion. Nat. Phys. **10**(10), 758–761 (2014)
231. Muller, U.K., van den Boogaart, J.G., van Leeuwen, J.L.: Flow patterns of larval fish: undulatory swimming in the intermediate flow regime. J. Exp. Biol. **211**(2), 196–205 (2008)
232. Cai, Y., Bi, S., Zheng, L.: Design and experiments of a robotic fish imitating cow-nosed ray. J. Bionic Eng. **7**(2), 120–126 (2010)
233. Clark, R.P., Smits, A.J.: Thrust production and wake structure of a batoid-inspired oscillating fin. J. Fluid Mech. **562**, 415–429 (2006)
234. Liu, G., Ren, Y., Zhu, J., Bart-Smith, H., Dong, H.: Thrust producing mechanisms in ray-inspired underwater vehicle propulsion. Theor. Appl. Mech. Lett. **5**(1), 54–57 (2015)
235. Moored, K.W., Smith, W., Hester, J., Chang, W., Bart-Smith, H.: Investigating the thrust production of a myliobatoid-inspired oscillating wing. In: Advances in Science and Technology, vol. 58, pp. 25–30 (2008). Trans Tech Publ
236. Azarsina, F.: Designing a hydrodynamic shape and thrust mechanism for a batoid underwater robot. Mar. Technol. Soc. J. **50**(5), 45–58 (2016)
237. Zhao, J., Mao, Q., Pan, G., Huang, Q., Sung, H.J.: Hydrodynamic benefit of cephalic fins in a self-propelled flexible manta ray. Phys. Fluids **33**(8), 081906 (2021)
238. Mittal, R., Dong, H., Bozkurttas, M., Lauder, G., Madden, P.: Locomotion with flexible propulsors: Ii. computational modeling of pectoral fin swimming in sunfish. Bioinspir. Biomimetics **1**(4), 35 (2006)
239. Tytell, E.D.: Kinematics and hydrodynamics of linear acceleration in eels, anguilla rostrata. Proc. R. Soc. Lond. Ser. B: Biol. Sci. **271**(1557), 2535–2540 (2004)
240. Novati, G., Verma, S., Alexeev, D., Rossinelli, D., Van Rees, W.M., Koumoutsakos, P.: Synchronisation through learning for two self-propelled swimmers. Bioinspir. Biomimetics **12**(3), 036001 (2017)
241. Khalid, M.S.U., Akhtar, I., Dong, H.: Hydrodynamics of a tandem fish school with asynchronous undulation of individuals. J. Fluids Struct. **66**, 19–35 (2016)
242. Barrett, D., Triantafyllou, M., Yue, D., Grosenbaugh, M., Wolfgang, M.: Drag reduction in fish-like locomotion. J. Fluid Mech. **392**, 183–212 (1999)
243. Khalid, M.S.U., Wang, J., Akhtar, I., Dong, H., Liu, M.: Modal decompositions of the kinematics of crevalle jack and the fluid-caudal fin interaction. Bioinspir. Biomimetics **16**(1), 016018 (2020)
244. White, C.H., Lauder, G.V., Bart-Smith, H.: Tunabot flex: a tuna-inspired robot with body flexibility improves high-performance swimming. Bioinspir. Biomimetics **16**(2), 026019 (2021)
245. Wang, S., Zhang, X., He, G.: Numerical simulation of a three-dimensional fish-like body swimming with finlets. Commun. Comput. Phys. **11**(4), 1323–1333 (2012)
246. Zhong, Q., Dong, H., Quinn, D.B.: How dorsal fin sharpness affects swimming speed and economy. J. Fluid Mech. **878**, 370–385 (2019)
247. Wang, J., Tran, H., Christino, M., White, C., Zhu, J., Lauder, G., Bart-Smith, H., Dong, H.: Hydrodynamics and flow characterization of tuna-inspired propulsion in forward swimming. In: Fluids Engineering Division Summer Meeting, vol. 59025, pp. 001–01025 (2019). American Society of Mechanical Engineers
248. Liu, H., Kawachi, K.: A numerical study of undulatory swimming. J. Comput. Phys. **155**(2), 223–247 (1999)
249. Von Ellenrieder, K.D., Parker, K., Soria, J.: Flow structures behind a heaving and pitching finite-span wing. J. Fluid Mech. **490**, 129–138 (2003)
250. Anderson, J.M., Streitlien, K., Barrett, D., Triantafyllou, M.S.: Oscillating foils of high propulsive efficiency. J. Fluid Mech. **360**, 41–72 (1998)
251. Koochesfahani, M.M.: Vortical patterns in the wake of an oscillating airfoil. AIAA J. **27**(9), 1200–1205 (1989)
252. Jones, K., Dohring, C., Platzer, M.: Experimental and computational investigation of the knoller-betz effect. AIAA J. **36**(7), 1240–1246 (1998)

253. Isogai, K., Shinmoto, Y., Watanabe, Y.: Effects of dynamic stall on propulsive efficiency and thrust of flapping airfoil. AIAA J. **37**(10), 1145–1151 (1999)
254. Tuncer, I.H., Platzer, M.F.: Computational study of flapping airfoil aerodynamics. J. Aircr. **37**(3), 514–520 (2000)
255. Mittal, R., Utturkar, Y., Udaykumar, H.: Computational modeling and analysis of biomimetic flight mechanisms. In: 40th AIAA Aerospace Sciences Meeting & Exhibit, p. 865 (2002)
256. Lewin, G.C., Haj-Hariri, H.: Modelling thrust generation of a two-dimensional heaving airfoil in a viscous flow. J. Fluid Mech. **492**, 339–362 (2003)
257. Guglielmini, L., Blondeaux, P.: Propulsive efficiency of oscillating foils. Eur. J. Mech.-B/Fluids **23**(2), 255–278 (2004)
258. Godoy-Diana, R., Marais, C., Aider, J.-L., Wesfreid, J.E.: A model for the symmetry breaking of the reverse bénard-von kármán vortex street produced by a flapping foil. J. Fluid Mech. **622**, 23–32 (2009)
259. Wong, J., Rival, D., et al.: Flow separation on flapping and rotating profiles with spanwise gradients. Bioinspir. Biomimetics **12**(2), 026008 (2017)
260. Mackowski, A., Williamson, C.: Direct measurement of thrust and efficiency of an airfoil undergoing pure pitching. J. Fluid Mech. **765**, 524–543 (2015)
261. Menon, K., Mittal, R.: Dynamic mode decomposition based analysis of flow over a sinusoidally pitching airfoil. J. Fluids Struct. **94**, 102886 (2020)
262. Zhu, Q.: Energy harvesting by a purely passive flapping foil from shear flows. J. Fluids Struct. **34**, 157–169 (2012)
263. Muscutt, L., Weymouth, G., Ganapathisubramani, B.: Performance augmentation mechanism of in-line tandem flapping foils. J. Fluid Mech. **827**, 484–505 (2017)
264. Chen, D., Kolomenskiy, D., Liu, H.: Closed-form solution for the edge vortex of a revolving plate. J. Fluid Mech. **821**, 200–218 (2017)
265. Hoover, A.P., Cortez, R., Tytell, E.D., Fauci, L.J.: Swimming performance, resonance and shape evolution in heaving flexible panels. J. Fluid Mech. **847**, 386–416 (2018)
266. Li, C., Dong, H.: Three-dimensional wake topology and propulsive performance of low-aspect-ratio pitching-rolling plates. Phys. Fluids **28**(7), 071901 (2016)
267. Han, J.-S., Chang, J.-W., Kim, S.-T.: Reynolds number dependency of an insect-based flapping wing. Bioinspir. Biomimetics **9**(4), 046012 (2014)
268. Han, J.-S., Chang, J.W., Han, J.-H.: The advance ratio effect on the lift augmentations of an insect-like flapping wing in forward flight. J. Fluid Mech. **808**, 485–510 (2016)
269. Green, M.A., Rowley, C.W., Smits, A.J.: The unsteady three-dimensional wake produced by a trapezoidal pitching panel. J. Fluid Mech. **685**, 117–145 (2011)
270. Shelton, R.M., Thornycroft, P.J., Lauder, G.V.: Undulatory locomotion of flexible foils as biomimetic models for understanding fish propulsion. J. Exp. Biol. **217**(12), 2110–2120 (2014)
271. Quinn, D.B., Lauder, G.V., Smits, A.J.: Maximizing the efficiency of a flexible propulsor using experimental optimization. J. Fluid Mech. **767**, 430–448 (2015)
272. Lehn, A.M., Thornycroft, P.J., Lauder, G.V., Leftwich, M.C.: Effect of input perturbation on the performance and wake dynamics of aquatic propulsion in heaving flexible foils. Phys. Rev. Fluids **2**(2), 023101 (2017)
273. Alben, S., Witt, C., Baker, T.V., Anderson, E., Lauder, G.V.: Dynamics of freely swimming flexible foils. Phys. Fluids **24**(5), 051901 (2012)
274. Blevins, E., Lauder, G.V.: Swimming near the substrate: a simple robotic model of stingray locomotion. Bioinspir. Biomimetics **8**(1), 016005 (2013)
275. Lucas, K.N., Thornycroft, P.J., Gemmell, B.J., Colin, S.P., Costello, J.H., Lauder, G.V.: Effects of non-uniform stiffness on the swimming performance of a passively-flexing, fish-like foil model. Bioinspir. Biomimetics **10**(5), 056019 (2015)
276. Jia, K., Fang, L., Huang, W.-X.: Coupled states of dual side-by-side inverted flags in a uniform flow. J. Fluids Struct. **91**, 102768 (2019)
277. Park, S.G., Sung, H.J.: Vortex interaction between two tandem flexible propulsors with a paddling-based locomotion. J. Fluid Mech. **793**, 612–632 (2016)
278. Park, S.G., Sung, H.J.: Hydrodynamics of flexible fins propelled in tandem, diagonal, triangular and diamond configurations. J. Fluid Mech. **840**, 154–189 (2018)
279. Van Dyke, M., Van Dyke, M.: An Album of Fluid Motion, vol. 176. Parabolic Press, Stanford (1982)
280. Jantzen, R.T., Taira, K., Granlund, K.O., Ol, M.V.: Vortex dynamics around pitching plates. Phys. Fluids **26**(5), 053606 (2014)
281. Shyy, W., Liu, H.: Flapping wings and aerodynamic lift: the role of leading-edge vortices. AIAA J. **45**(12), 2817–2819 (2007)
282. Harbig, R.R., Sheridan, J., Thompson, M.C.: Reynolds number and aspect ratio effects on the leading-edge vortex for rotating insect wing planforms. J. Fluid Mech. **717**, 166–192 (2013)
283. Chen, D., Kolomenskiy, D., Nakata, T., Liu, H.: Forewings match the formation of leading-edge vortices and dominate aerodynamic force production in revolving insect wings. Bioinspir. Biomimetics **13**(1), 016009 (2017)
284. Ma, M., Huang, W.X., Xu, C.X.: A dynamic wall model for large eddy simulation of turbulent flow over complex/moving boundaries based on the immersed boundary method. Phys. Fluids **31**(11), 115101 (2019)
285. Ma, M., Huang, W.X., Xu, C.X., Cui, G.X.: A hybrid immersed boundary/wall-model approach for large-eddy simulation of high-reynolds-number turbulent flows. Int. J. Heat Fluid Flow **88**, 108769 (2021)
286. Triantafyllou, M., Triantafyllou, G., Gopalkrishnan, R.: Wake mechanics for thrust generation in oscillating foils. Phys. Fluids A **3**(12), 2835–2837 (1991)
287. Saadat, M., Fish, F.E., Domel, A., Di Santo, V., Lauder, G., Haj-Hariri, H.: On the rules for aquatic locomotion. Phys. Rev. Fluids **2**(8), 083102 (2017)
288. Rohr, J.J., Fish, F.E.: Strouhal numbers and optimization of swimming by odontocete cetaceans. J. Exp. Biol. **207**(10), 1633–1642 (2004)

289. Floryan, D., Van Buren, T., Smits, A.J.: Efficient cruising for swimming and flying animals is dictated by fluid drag. Proc. Natl. Acad. Sci. **115**(32), 8116–8118 (2018)
290. Sfakiotakis, M., Lane, D.M., Davies, J.B.C.: Review of fish swimming modes for aquatic locomotion. IEEE J. Oceanic Eng. **24**(2), 237–252 (1999)
291. Fish, F.E., Lauder, G.V.: Control surfaces of aquatic vertebrates: active and passive design and function. J. Exp. Biol. **220**(23), 4351–4363 (2017)
292. Walker, J.A.: Does a rigid body limit maneuverability? J. Exp. Biol. **203**(22), 3391–3396 (2000)
293. Hove, J., O'Bryan, L., Gordon, M.S., Webb, P.W., Weihs, D.: Boxfishes (teleostei: Ostraciidae) as a model system for fishes swimming with many fins: kinematics. J. Exp. Biol. **204**(8), 1459–1471 (2001)
294. Bartol, I.K., Gharib, M., Weihs, D., Webb, P.W., Hove, J.R., Gordon, M.S.: Hydrodynamic stability of swimming in ostraciid fishes: role of the carapace in the smooth trunkfish lactophrys triqueter (teleostei: Ostraciidae). J. Exp. Biol. **206**(4), 725–744 (2003)
295. Bartol, I.K., Gharib, M., Webb, P.W., Weihs, D., Gordon, M.S.: Bodyinduced vortical flows: a common mechanism for self-corrective trimming control in boxfishes. J. Exp. Biol. **208**(2), 327–344 (2005)
296. Bartol, I.K., Gordon, M.S., Webb, P., Weihs, D., Gharib, M.: Evidence of self-correcting spiral flows in swimming boxfishes. Bioinspir. Biomimetics **3**(1), 014001 (2008)
297. Blake, R.: On ostraciiform locomotion. J. Mar. Biol. Assoc. UK **57**(4), 1047–1055 (1977)
298. Van Wassenbergh, S., van Manen, K., Marcroft, T.A., Alfaro, M.E., Stamhuis, E.J.: Boxfish swimming paradox resolved: forces by the flow of water around the body promote manoeuvrability. J. R. Soc. Interface **12**(103), 20141146 (2015)
299. Mistick, E.A., Mountcastle, A.M., Combes, S.A.: Wing flexibility improves bumblebee flight stability. J. Exp. Biol. **219**(21), 3384–3390 (2016)
300. Zhu, H.J., Meng, X.G., Sun, M.: Forward flight stability in a drone-fly. Sci. Rep. **10**(1), 1–12 (2020)
301. Sarradj, E., Fritzsche, C., Geyer, T.: Silent owl flight: bird flyover noise measurements. AIAA J. **49**(4), 769–779 (2011)
302. Jackson, J.C., Robert, D.: Nonlinear auditory mechanism enhances female sounds for male mosquitoes. Proc. Natl. Acad. Sci. **103**(45), 16734–16739 (2006)
303. Srygley, R.B.: Evolution of the wave: aerodynamic and aposematic functions of butterfly wing motion. Proc. R. Soc. B: Biol. Sci. **274**(1612), 913–917 (2007)
304. Jaworski, J.W., Peake, N.: Aeroacoustics of silent owl flight. Annu. Rev. Fluid Mech. **52**, 395–420 (2020)
305. Ji, X., Wang, L., Ravi, S., Tian, F.-B., Young, J., Lai, J.C.: Influences of serrated trailing edge on the aerodynamic and aeroacoustic performance of a flapping wing during hovering flight. Phys. Fluids **34**(1), 011902 (2022)
306. Wang, L., Tian, F.-B.: Numerical study of flexible flapping wings with an immersed boundary method: Fluid-structure-acoustics interaction. J. Fluids Struct. **90**, 396–409 (2019)
307. Wang, L., Tian, F.-B.: Numerical study of sound generation by three-dimensional flexible flapping wings during hovering flight. J. Fluids Struct. **99**, 103165 (2020)
308. Geng, B., Xue, Q., Zheng, X., Liu, G., Ren, Y., Dong, H.: The effect of wing flexibility on sound generation of flapping wings. Bioinspir. Biomimetics **13**(1), 016010 (2017)
309. Seo, J.-H., Hedrick, T.L., Mittal, R.: Mechanism and scaling of wing tone generation in mosquitoes. Bioinspir. Biomimetics **15**(1), 016008 (2019)
310. Seo, J.-H., Hedrick, T.L., Mittal, R.: Mosquitoes buzz and fruit flies don'ta comparative aeroacoustic analysis of wing-tone generation. Bioinspir. Biomimetics **16**(4), 046019 (2021)
311. Wagenhoffer, N., Moored, K.W., Jaworski, J.W.: Unsteady propulsion and the acoustic signature of undulatory swimmers in and out of ground effect. Phys. Rev. Fluids **6**(3), 033101 (2021)
312. Zhu, Y., Tian, F.-B., Young, J., Liao, J.C., Lai, J.C.: A numerical study of fish adaption behaviors in complex environments with a deep reinforcement learning and immersed boundary-lattice boltzmann method. Sci. Rep. **11**(1), 1–20 (2021)
313. Zhu, Y., Pang, J.-H., Tian, F.-B.: Stable schooling formations emerge from the combined effect of the active control and passive self-organization. Fluids **7**(1), 41 (2022)